TWO- AND THREE-DIMENSIONAL METAMATERIALS FOR THE INFRARED SPECTRAL RANGE

by

Micheal J. McLamb

A dissertation submitted to the faculty of
The University of North Carolina at Charlotte
in partial fulfillment of the requirements
for the degree of Doctor of Philosophy in
Optical Science and Engineering

Charlotte

2024

Approved by:

_____
Dr. Tino Hofmann

_____
Dr. Glenn D. Boreman

_____
Dr. Menelaos K. Poutous

_____
Dr. Andrew R. Willis

ABSTRACT

MICHEAL J. MCLAMB. Two- and Three-Dimensional Metamaterials for the Infrared Spectral Range. (Under the direction of DR. TINO HOFMANN)

Plasmonic metamaterials are artificially structured materials with the inclusion of metallic elements regarded as macroscopically uniform mediums. These materials showcase adaptable optical characteristics achieved through manipulation of the materials' intrinsic geometries at scales much finer than the wavelength of the incident electromagnetic radiation under consideration.

This dissertation focuses on the fabrication methodologies and applications of plasmonic metamaterials in perfect absorption and plasmonic sensing. Plasmonic metamaterials, distinguished by their ability to manipulate electromagnetic radiation through engineered subwavelength structures, have garnered significant attention for their potential in various fields, including photonics, sensing, and energy harvesting.

The dissertation examines current fabrication techniques for plasmonic metamaterials, focusing on additive manufacturing approaches. The advantages of two-photon polymerization for the fabrication of plasmonic metamaterials is discussed in detail along with more traditional techniques like electron beam vapor deposition and atomic layer deposition. The advantages and limitations of each approach are scrutinized, laying the groundwork for subsequent investigations into tailored designs for specific applications.

Building upon the foundation of fabrication techniques, two distinct applications of plasmonic metamaterials are examined. Firstly, the concept of perfect absorption, wherein the metamaterial is engineered to efficiently absorb incident electromagnetic radiation across a narrow spectral range. Through theoretical modeling and experimental validation, novel designs for achieving perfect absorption are proposed and characterized. The investigated designs leverage the unique optical properties of plas-

monic metamaterials to enhance light-matter interactions.

Subsequently, the utilization of these architectures for sensing applications is demonstrated. By exploiting the sensitivity of surface plasmon resonance to changes in the local refractive index, plasmonic metamaterials offer unprecedented opportunities for label-free, real-time detection of biomolecules, gases, and other analytes.

This dissertation showcases the potential practical applications of plasmonic metamaterials in perfect absorption and plasmonic sensing. It contributes to the ongoing advancement of plasmonic metamaterials and their seamless integration into cutting-edge photonics and sensing technologies.

DEDICATION

I dedicate this dissertation and work to my family and friends. I would like to thank my wife for her love, support, and for putting up with me. She has been my rock when I needed support and a fire at my behind when I needed motivation. To my grandmother, thank you for your words of wisdom and counsel. She has always been there to say what I needed to hear most, even when I did not want to hear it. Thanks to my grandfather and uncle who are my role-models. I still aspire to attain their level of discipline.

ACKNOWLEDGEMENTS

I extend my heartfelt gratitude to all the individuals who have played a pivotal role in making this academic journey possible and unforgettable. I firmly believe that the whole is indeed the sum of its parts, and I am deeply grateful for the multitude of contributions from friends and mentors that have shaped my path.

I am deeply grateful to Prof. Tino Hofmann for his unwavering support, guidance, and friendship throughout my academic journey. Tino, you have not only been my advisor and mentor but also a cherished friend. Your dedication to my growth and development has been truly inspiring. You have consistently encouraged me to step out of my comfort zone, think critically, and strive for excellence in all endeavors.

As the saying goes, "the more time you spend with your advisor, the more you start to become them." In this regard, I consider myself incredibly fortunate to have had Tino as my advisor. Your influence has played a significant role in shaping my academic and personal growth. I could not have asked for a better mentor to guide me through the challenges and triumphs of graduate school.

I am deeply indebted to Yanzeng Li, whose guidance and mentorship were instrumental during my early days in Tino's lab. Yanzeng patiently imparted invaluable knowledge, from navigating simulation software to mastering the intricacies of sample fabrication and measurement techniques. I vividly recall the countless hours spent alongside him, eagerly absorbing every word and learning the ropes of research. Some of my most cherished memories revolve around our late-night sessions, the camaraderie shared in the cleanroom, and the exhilarating moment of achieving my first proof of concept and subsequent publication. Without Yanzeng's foundational work and unwavering support, this dissertation would not have come to fruition.

I would also like to extend my heartfelt gratitude to Serang Park, whose infectious enthusiasm and boundless energy breathed life into our group dynamic. Her presence, though missed after her graduation, served as a constant source of inspiration and

motivation. I am thrilled to see her thriving, and I remain grateful for the indelible impact she left on our lab culture.

I am immensely grateful to Paige Stinson, who has become a dear friend and colleague. From the moment Paige joined our group, her dedication and enthusiasm have been truly inspiring. She seamlessly integrated into our team and quickly demonstrated her exceptional abilities. Paige's relentless pursuit of excellence and her knack for generating innovative ideas have consistently yielded remarkable results. It has been a privilege to witness her growth, achievements, and well-deserved recognition within our academic community.

I am also delighted to welcome Nuren Shuchi and Dustin Louisos, the newest members of our lab. Their intelligence, motivation, and commitment to excellence are evident from the outset, and I am excited to see how their contributions will shape the future of our research endeavors at the university.

I extend my heartfelt gratitude to Prof. Glenn Boreman for his pivotal role in shaping my academic journey. Prof. Boreman's thoughtful gesture of informing me about Tino's search for a student has had a profound impact on my life. Without his kind words and guidance, I would not have had the opportunity to forge lasting friendships and pursue my passion for research. I am indebted to Dr. Boreman for opening the door that led to life-changing opportunities and experiences. Thank you, Prof. Boreman, for your generosity, support, and belief in my potential. Your influence will forever be cherished in my academic and personal endeavors.

I am deeply grateful to Dr. Joshua Lentz for providing me with the opportunity to advance my research at the university. His support and mentorship have been invaluable throughout my academic journey. Dr. Lentz not only offered guidance on navigating the intricacies of research but also provided invaluable advice regarding my future career path. His sponsorship and unwavering belief in my abilities have been instrumental in shaping my academic and professional endeavors. I am truly

appreciative of his unique insight, which has played a pivotal role in my growth and success during my last years of study. Thank you, Joshua Lentz, for your exceptional support, mentorship, and encouragement.

I would like to express my sincere gratitude to Prof. Menelaos Poutous for serving on my committee. Prof. Poutous's insights and contributions to my committee have been invaluable, and I am grateful for the opportunity to benefit from his expertise. His guidance has not only enriched my academic experience but has also contributed significantly to my professional growth. Thank you, Prof. Poutous, for your unwavering dedication to excellence and for your role in shaping my academic journey. Your mentorship has been truly appreciated.

My heartfelt gratitude goes to Prof. Andrew Willis for his invaluable contributions to my dissertation committee. Working alongside Prof. Willis at the Center for Metamaterials has been a pleasure and a privilege. His insights, expertise, and dedication have enriched our collaborative efforts and enhanced the quality of my research.

In closing, I extend my deepest gratitude to all those who have contributed to my academic journey and the completion of this dissertation. Your support, guidance, and encouragement have been instrumental in shaping my growth and achievements. I am profoundly grateful for the collaborative efforts, unwavering encouragement, and enduring friendships that have enriched this experience.

TABLE OF CONTENTS

LIST OF TABLES

LIST OF FIGURES

CHAPTER 1: Introduction

1.1 Overview

Several metamaterial designs are presented in this work that have potential applications in perfect absorption, polarization selective reflectance, and ambient refractive index sensing as well as a fabrication process for the rapid prototyping of plasmonic metamaterials using additive manufacturing. The initial chapter details the fabrication process for a simple arrangement of metallic bars to create a polarization sensitive reflector which is further altered to create a metasurface that displays two separate images depending of the linear polarization of the source. The reciprocal plasmonic metasurface is a perfectly absorbing metamaterial that displays sensitivity to changes in the ambient index.

Metamaterials are a group of materials that are designed to manipulate amplitude, phase, and polarization of incident electromagnetic radiation through spatially periodic arrangement of sub-wavelength optical elements [1]. Plasmonic metamaterials are a subset of metamaterials which utilizes the collective oscillation of electrons on the surface of a metal known as a surface plasmon polariton. Tuning these metallic elements such that incident radiation induces these polaritons leads to localization and enhancement of the electromagnetic fields [2].

The concept of a metamaterial was first alluded to by Russian scientist Victor Veselago in 1968. Veselago asserted that the permitivity and permeability (ε, μ) $\not<$ 0 for materials found in nature and suggested that negative refractive index would occur if these values were to be simultaneously negative [3]. In the year 2000, Sir John Pendry published a brief journal article expanding on Veselago's work and suggested a mechanism for creating a perfectly focusing lens utilizing negative refractive

index [4]. In 2006, the first experimental demonstration of a functional metamaterial is produced by David Smith in collaboration with Sir Pendry *et. al.* in the form of a microwave cloaking device [5]. Metamaterial research has since been driven by designing optical components to perform in ways previously thought to be impossible. Metamaterial capabilities have expanded from a perfect lens and cloaking to energy harvesting, optical filters, sensors, super-resolution lenses, and thermal emission control, for instance. Fabrication methods and computing power of simulations have prevented the effectuation of such devices in the past but new fabrication techniques and ever-growing capabilities of computers have emerged allowing for the realization of working metamaterials.

Fabrication of metamaterials includes both additive and substractive techniques. Examples of subtractive manufacturing include laser cutting, CNC machining, water-jet cutting, and lithography to name a few. Additive manufacturing techniques include, two-photon polymerization, material extrusion, and material jetting. There are advantages and disadvantages for both fabrication processes. Advantages of substractive manufacturing include the number of suitable materials available, high surface accuracy, and the lack of post-processing required. On the other hand, substractive manufacturing may not be able to produce geometries with higher complexity and leaves material waste that may become expensive. Additive manufacturing provides a fast and cheap alternative allowing for the rapid prototyping of metamaterials for a research environment at the cost of manufacturing scalability [6]. This work will focus on several metamaterial designs and the additive manufacturing processes used to fabricate them.

1.2 Modeling

Finite element modeling (FEM) is employed to predict the optical response of the various designs of metamaterials that are described in the following chapters. FEM is a numerical method of solving partial differential equations within a two- or three-

dimensional space. These calculations are performed by demarcating sections of the space with imposed boundary conditions referred to as finite elements to create a mesh. The dimensions of these individual elements are determined in several different ways. In the steady state case, elements are modeled using algebraic equations that locally approximate the original complex partial differential equations of the entire system.

A generic overview of the modeling process consists of an inclusion of accurate dielectric function data and the desired geometry. Accurate knowledge of the optical properties of included materials is essential for the design and fabrication of structured optical materials. Here we use spectroscopic ellipsometry as a precision optical characterization technique that monitors changes in the polarization state and phase of incident electromagnetic radiation on a given sample composed of stratified components. Measuring this change yields ellipsometric parameters Ψ and Δ which describe the amplitude ratio and difference in phase between the p- and s- polarized reflections respectively. This measurement technique is sensitive to the thickness of the sample constituents and their optical properties. As the thickness increases, there is an increasing optical path difference. Allowing for a stratified model fitting (J. A. Woollam's WVASE) of optical properties and sample geometry independent of one another [7].

All material properties utilized in FEM calculations are characterized with spectroscopic ellipsometry ranging from 2 µm - 30 µm using J. A. Woollam's IR-VASE. The majority of simulated constituents composing the metamaterials in this work consist of Nanoscribe's fused silica, electron-beam deposited Au, air, and Nanoscribe's IP-Dip for the case of single-photon polymerization.

The FEM modeling uses a square unit cell with a fused silica substrate with the desired geometry resting on the substrate plane. The four sides of the unit cell are configured with periodic boundary conditions to simulate an infinite array of

sub-wavelength structures. The emitting port is placed above the desired structure at an arbitrary distance and a receiver placed in the base plane of the substrate. Perfectly matched layers are included above and below the emitting and receiving port respectively. A perfectly matched layer mimics a non-reflective interface into an infinite domain. These perfectly matched layers also contain scattering conditions. These settings ensure that once light interacts with the unit cell, including Fresnel reflections, all transmitted light and reflected light escapes the system.

1.3 Fabrication

Two distinct sample geometries are investigated in this work. One geometry is a two dimensional arrangement of subwavelength features the second is a three dimensional arrangement of two dimensional surfaces separated by a dielectric spacer.

The bulk of the sample fabrication is performed using additive manufacturing techniques. Two-photon polymerization is a photo-chemical process wherein the advantage lies in the non-linear absorption of the photon. This allows for substrate plane resolution on the order of 100 nm as well as arbitrary geometry construction. Considering this spatial resolution, this process is sufficient to fabricate sub-wavelength structures necessary for metamaterials operating in the near- to mid- infrared. Here we use Nanoscribe's Photonic Professional GT2 that employs a linear writing process and is not suitable for commercial manufacturing. However, this technique excels in rapidly prototyping samples in lab-based research to provide insight into a sample's operating mechanisms and provide proof on concept.

The architecture of the sub-wavelength features of the sample dictate how the three-dimensional direct laser writing will be utilized. In the case of the presented two-dimensional plasmonic materials, an inverse thin layer of the desired geometry will be written and removed after metallization leaving only the desired geometry on the substrate. For the case of three-dimensional plasmonic materials, the polymer layer serves as a scaffold suspending one metallic layer above another.

One metallic constituent, Au, was used in all of the following metamaterial designs. Au layers were deposited onto existing polymer scaffolds or inverse polymer layers using electron beam physical vapor deposition via Kurt J. Lesker's PVD 75 system at approximate pressures of 5×10^{-8} Torr. Electron beam deposition is a line of sight deposition process. It is therefore not suitable for complex three-dimensional geometries that require coatings in a location that is in the "shadow" cast by the polymer scaffold. In the case of the metamaterials shown here, a line of sight method is preferred for creating metallic layers.

Atomic layer deposition (ALD) is employed here to attain conformal coatings of dielectrics on complex three-dimensional metamaterials, ALD is a subclass of the chemical vapor deposition (CVD) process with the difference pertaining to how precursors react. In CVD, volatile precursors are injected into the reaction chamber under vacuum at the same time to react and degrade resulting in a thin film. The precursors saturate the surface of a heated substrate where nucleation of the precursors begin to aggregate randomly. In contrast, the majority of ALD procedures are based on binary reaction sequences, in which two surface reactions take place, and a compound film is formed. The reactions can only deposit a limited number of surface species dictated by the surface area of the substrate. Because each surface reaction is self-limiting, it can be performed in sequential order [8]. Though it is a slower deposition process than CVD the main advantage of the technique is the capability to deposit conformal thin films. There are several subsets of ALD pertaining to how the reaction takes place, such as thermal, plasma-assisted, and spatial ALD. This work will focus on the thermal oxidation process where the chemical reaction takes place at the substrate surface.

REFERENCES

[1] F. Ding, "A Review of Multifunctional Optical Gap-Surface Plasmon Metasurfaces," *Pr. Electromagn. Res. S.* **174**, pp. 55-73 (2022).

[2] T. Gric and E. Rafailov, "Propagation of surface plasmon polaritons at the interface of metal-free metamaterial with anisotropic semiconductor inclusions," *Optik* **254**, p. 168678 (2022).

[3] V. Veselago, "The Electrodynamics of Substances with Simultaneously Negative Values of ε and μ," *Sov. Phys. Usp.* **10**, pp. 509-514 (1968).

[4] J. B. Pendry, "Negative refraction makes a perfect lens," *Phys. Rev. Lett.* **85**, p. 3966 (2000).

[5] D. Schurig, J. J. Mock, B. J. Justice, S. A. Cummer, J. B. Pendry, A. F. Starr, and D. R. Smith, "Metamaterial electromagnetic cloak at microwave frequencies," *Science* **314**, pp. 977-980 (2006).

[6] Z. Chen, Y.-T. Lin, H. Salehi, Z. Che, Y. Zhu, J. Ding, B. Sheng, R. Zhu, and P. Jiao, "Advanced Fabrication of Mechanical Metamaterials Basedon Micro/Nanoscale Technology," *Adv. Eng. Mater.* **25**, p. 2300750 (2023).

[7] J. A. Woollam, C. L. Bungay, L. Yan, D. W. Thompson, and J. N. Hilfiker, "Application of spectroscopic ellipsometry to characterization of optical thin films," *Laser-Induced Damage in Optical Materials: 2002 and 7th International Workshop on Laser Beam and Optics Characterization* **4932**, pp. 393-404 (2003). SPIE.

[8] T. J. Kunene, L. K. Tartibu, K. Ukoba, T.-C. Jen "Review of atomic layer deposition process, application and modeling tools," *Mater. Today-Proc.* **62**, pp. S95-S109 (2022).

CHAPTER 2: Metasurfaces for the infrared spectral range fabricated using two-photon polymerization

2.1 Overview

Fabrication of metasurfaces is often time consuming and expensive, involving complex lithographic processes.[1] The maskless fabrication of metasurfaces composed of rectangular Au bars is reported as a suitable alternative, providing cost-effective, rapid prototyping of metasurfaces. The investigated metasurfaces were fabricated using a simple three-step process which is discussed in detail. The fabrication process establishes a simple method for producing high fidelity 2D patterns suitable to synthesize metasurfaces for chemical sensing, beam steering, and perfect reflection/transmission. Comprehensive polarization-sensitive reflection data reveal multiple resonances in the infrared spectral range. In addition to the dipole and substrate resonances, a resonance which is attributed to a coupling between the excitation of the metasurface and the substrate phonon mode is observed.

2.2 Introduction

Metamaterials describe a group of materials designed to have properties typically not found or existing in naturally occurring compounds [1]. The optical properties of metamaterials can be tuned by the shape, geometric parameters, composition, and the arrangement of their constituents [2, 3, 4, 5, 6, 7].

Metasurfaces are 2D metamaterials which have drawn substantial attention in recent years due to their ability to provide large local electromagnetic field improve-

[1] Reprinted by permission from Elsevier Inc. M. McLamb, Y. Li, P. Stinson, and T. Hofmann, "Metasurfaces for the infrared spectral range fabricated using two-photon polymerization," *Thin Solid Films* **721**, 138548 (2021).© 2021

ments for directivity, surface-enhanced Raman scattering, and vibrational mode coupling, for instance [8, 9, 10]. Plasmonic metasurfaces are a subset of metasurfaces for which a coupling with localized surface plasmon excitations further improves the electromagnetic characteristics of the metasurface [8].

Metasurfaces have been demonstrated using a wide range of constituents from nanorods, nanodots, to nanobars for which high sensitivity photodetection, hot electron collection, and biosensing has been observed [11]. There are also promising applications in energy harvesting, thermal imaging, and thermal emission [11, 12]. Au nanobars have recently been used in plasmonic sensing where they are superior to traditional structures by offering advantages in parameter control through changes in structure and index [11].

Several different fabrication methods ranging from photolithography, E-beam deposition, etching, and lift-off to laser induced forward transfer approaches, have been explored for the fabrication of metasurfaces [8, 13, 14]. In addition, significant progress has been made in enhancing the fabrication scale of these metasurfaces using self-assembly processes [13]. While self-assembly processes, in principle, allow scaling to larger metasurface areas, the accessible constituent geometries are often limited.

Recently, direct laser writing using two-photon polymerization has been explored for the fabrication of metasurfaces [10, 13, 14]. This approach has the advantage that it does not require the use of expensive lithographic masks and therefore reduces fabrication time and cost. It further enables the rapid prototyping of metasurfaces with different constituent geometries.

In this study we report on the fabrication and polarization optical characterization of metasurfaces in the infrared spectral range. The fabrication concept presented here further simplifies the two-photon polymerization configuration and improves the quality of the fabricated metasurfaces compared to previously used approaches [10].

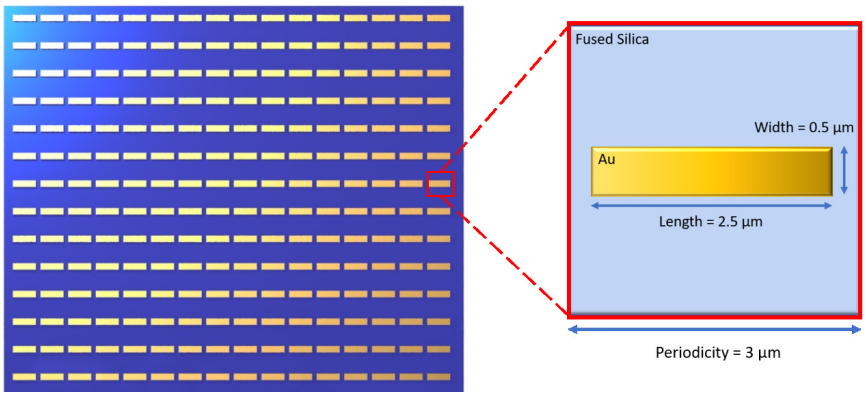

Figure 2.1: The metasurface geometry studied here is composed of Au bar resonators positioned in a square unit cell on a silica substrate. The inset shows a magnified view of the unit cell. The optimal geometric parameters for a dipole resonance centered at 6 µm were found using finite element model simulations (length = 2.5 µm, width = 0.5 µm, and periodicity = 3 µm). The thickness of the Au bar resonators is 50 nm.

2.3 Design and Fabrication

Finite element model simulations were performed using COMSOL in order to determine the optimal geometric parameters of a metasurface composed of bar resonators to produce a strong dipole resonance in the infrared spectral range. The calculations were carried out using periodic boundary conditions with a unit cell as shown in the inset of Fig. 2.1. The unit cell consists of a single rectangular Au bar resonator, the fused silica substrate, and ambient air.

Accurate dielectric function data were obtained for the fused silica substrate (Nanoscribe GmbH) using ellipsometric measurements in the range from 2 µm - 33 µm (IR-Vase, J.A. Woollam Co., Inc.) and imported into COMSOL. A single-term Drude model is employed here to describe the dielectric response of Au in the spectral range from 2 µm to 16 µm. The Drude model parameters are $\rho_1 = (3.3 \pm 3 \times 10^{-7}) \times 10^{-6}$ Ω/cm, $\tau_1 = (18 \pm 1.13)$ fs. The optical response has been verified through infrared spectroscopic ellipsometry in the spectral range from 2 µm to 33 µm using a witness sample. The dielectric function for fused silica and Au is depicted in Fig. 2.2 (a) and (b), respectively.

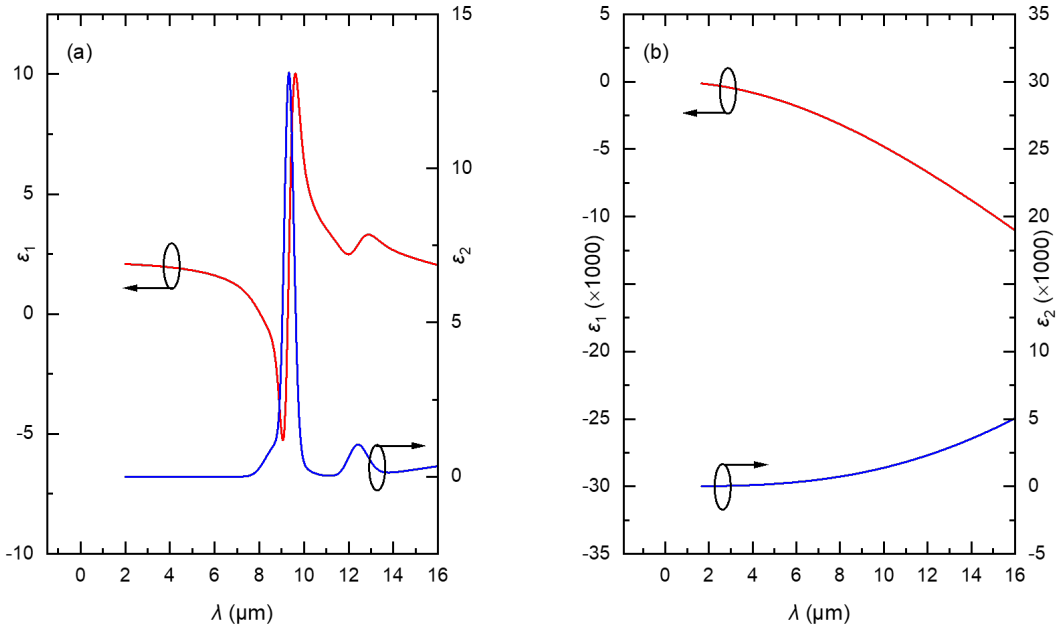

Figure 2.2: Real and imaginary dielectric function data ϵ_1 and ϵ_2, respectively, obtained via spectroscopic ellipsometry ranging from 2 µm to 16 µm of (a) fused silica substrate and (b) Au deposited via electron beam evaporation onto a fused silica substrate witness sample.

The width and length of the rectangular dipole as well as the periodicity of the array were varied in order to determine dimensions that would yield a resonance centered at 6 µm. The height of the resonators was held at a constant 38 nm, which was determined experimentally by spectroscopic ellipsometry using a fused silica substrate witness sample. As a result, the bar resonator length and width were determined to be 2.5 µm and 0.5 µm, respectively.

The investigated metasurfaces were fabricated using a three-step process onto fused silica substrates ((25 × 25) mm^2, 700 µm thick, Nanoscribe GmbH) which were cleaned prior to the deposition by rinsing with isopropanol-2 and drying with N_2. First, a patterned sacrificial negative-tone photoresist (IP-Dip) layer was deposited using a two-photon polymerization process, which allows its maskless fabrication. The sacrificial layer has a thickness of 200 nm and is inversely patterned to the

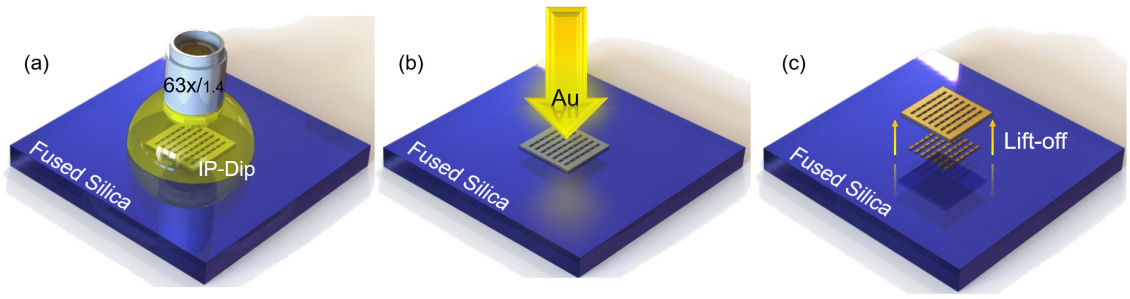

Figure 2.3: Illustration of the three fabrication steps employed here to synthesize metasurfaces. (a) A sacrificial layer of the inverse desired metasurface geometry is fabricated using two-photon polymerization (Photonic Professional (GT), GmbH) with a 63× objective lens immersed in a two-photon polymerization compatible photoresist: IP-Dip (Nanoscribe GmbH). (b) After the polymerization and development of the inverse geometry, a thin Cr adhesion layer and a Au film are deposited using e-beam evaporation. (c) Subsequent to the metallization step, the sacrificial layer is removed leaving only the structured Au metasurface with the desired geometry on the fused silica substrate.

metasurface depicted in Fig. 2.1. This step is followed by metallization and subsequent sacrificial layer lift-off. A schematic detailing the process steps for the fabrication of the metasurface can be observed in Fig. 2.3.

A commercial two-photon lithography system (Photonic Professional GT, Nanoscribe GmbH) was employed for the patterning of the sacrificial layer. The instrument utilizes a 780 nm femtosecond laser in conjunction with an inverted microscope and a 63x immersion objective. High resolution direct laser writing is achieved by inducing the absorption of two photons [15]. This non-linear process results in the polymerization of a spherical volume with a diameter of approximately 200 nm [10, 15, 16].

The position of the voxel in the x-y plane is determined by the motorized sample stage while the objective is fixed. Further control of the voxel position is achieved by manipulating the beam using a galvanometer. This allows the position of the voxel to be adjusted within a circular area in the x-y plane with a diameter of approximately 200 µm. For the fabrication of the patterned sacrificial layer the vertical voxel position was at the interface of the substrate and the IP-Dip monomer with

no additional changes in the vertical voxel position made. To ensure highest pattern fidelity and interface adhesion the exposure parameters were optimized prior to the sacrificial layer fabrication by adjusting laser power and write speed [17, 18]. Using the optimized fabrication parameters the processing of the sacrificial layer can be achieved in approximately 30 minutes.

After polymerization, excess IP-Dip monomer is removed from the substrate by vertically immersing the sample into propylene glycol monomethyl ether acetate for two minutes and then into isopropanol-2 for two minutes. Once the excess monomer has been removed the sample is allowed to air dry at room temperature for approximately 5 minutes.

After the direct laser writing of the patterned sacrificial layer is completed, the sample was metallized (Kurt J. Lesker PVD 75). Initially, electron beam evaporation was used to deposit a 7 nm adhesion layer of chromium, sourced from chromium pieces (99.95%) and, immediately following, a 38 nm Au layer (determined experimentally using spectroscopic ellipsometry) evaporated from Au pellets (99.99%). Both films were deposited at a rate of 1 Å/s. All depositions were carried out at room temperature at a pressure of 2.53×10^{-5} Pa. The substrate holder was rotated during the deposition at approximately 15 rpm to ensure a homogeneous film thickness across the entire sample.

After the metallization, the sacrificial photoresist layer was removed by plasma cleaning at 150 watts and a 12 SCCM flow of O_2 (Tergeo Plus, Pie Scientific). After the plasma cleaning the substrate is completely immersed in acetone until the sacrificial photoresist layer is lifted off completely. Subsequently, the sample is cleaned by rinsing with isopropanol-2 and methanol and dried with N_2.

The metasurface was characterized using polarized infrared reflection measurements in order to determine its infrared optical response. Complementary scanning electron microscope images (JEOL 6460LV), with an operating voltage of 14 kV, were obtained

in order to verify the dimensions and integrity of the fabricated metasurface.

Linearly polarized reflectance data was captured using a Hyperion 3000 microscope (Bruker) in combination with a Vertex 70 FTIR spectrometer (Bruker). The reflectance measurements were carried out in the spectral range of 2 µm to 16 µm with a resolution of 0.05 µm. A 15x IR Schwarzschild objective and a mercury cadmium telluride detector were used for all measurements. An adjustable, KRS-5, wire-grid polarizer mounted in a custom-built, electro-mechanical, rotation stage was used to polarize the incident radiation.

2.4 Results & Discussion

Fig. 2.4 depicts a scanning electron micropscope (SEM) micrograph top-view of the fabricated metasurface. As can be clearly observed, the rectangular bar resonators were fabricated with high fidelity. In particular the true-to-design geometry of the rectangular resonator bars is notable if compared to similar structures obtained with different lithographic techniques [10, 13]. The dimensions of the fabricated bar resonators are found to be in good agreement with the nominal values shown in Fig. 2.1. Analysis of the SEM micrograph reveals a length of the long and short axis of the bar resonators of 2.3 µm and 0.5 µm, respectively, which is in good agreement with the nominal design values of the long and short axes. Furthermore, the dimensions of the bar resonators are homogeneous across the metasurfaces.

The experimental infrared reflection data are compared with finite element model based calculated reflection data. The experimental (green dashed lines) and finite element model calculated (red solid lines) reflectance spectra in Fig. 2.5 panels (a) and (b) display the response of the bar resonators to linearly polarized light along the long and short axes, respectively. Overall, a good agreement between the model calculated and the experimental data can be observed. All the major spectral features and their relative magnitudes are reproduced accurately by the model calculation. An offset can be noticed at the lower and upper end of the spectral range. The reflectance

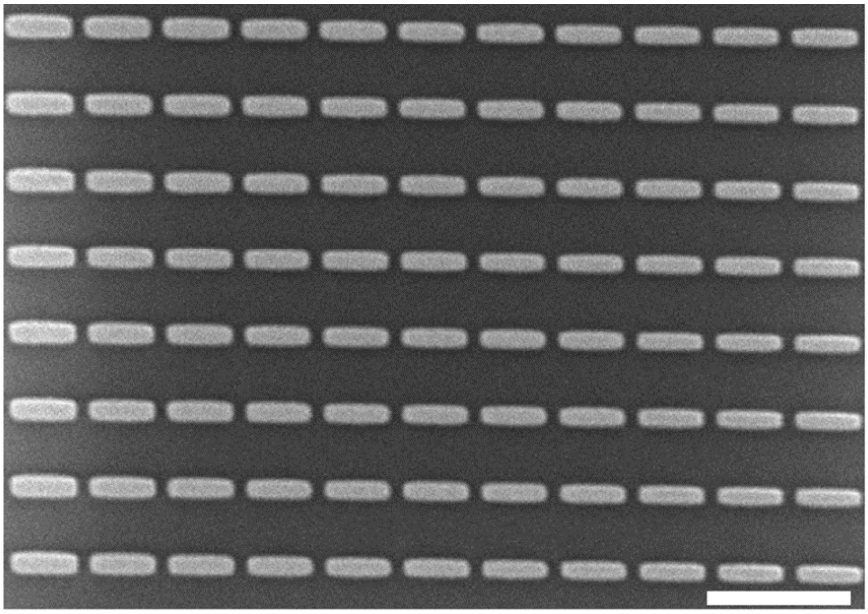

Figure 2.4: Top-view SEM micrograph of the metasurface depicting the regular arrangement of the rectangular bar resonators. The scale bar at the bottom right indicates 5 µm. The bar resonator has a long axis length of 2.3 µm and a short axis length of 0.5 µm.

in the vicinity of these strong spectral resonances is considerably underestimated. A better agreement with the experimental reflectance data in the spectral range outside of these areas can be achieved using simple stratified optical layer calculations which consider the average metal coverage due to the Au bar array.

When the light is polarized along the long axis three distinctive peaks can be observed. The first peak, located at 6 µm, is due to the dipole resonance of the bar resonator. This resonance is polarization sensitive as can be seen by comparing the reflectance spectra in Fig. 2.5 panels (a) and (b). While the resonance is dominating the reflectance spectrum obtained with the input polarization oriented parallel to the long axis of the resonator Fig. 2.5 (a), it is completely suppressed for the perpendicular orientation Fig. 2.5 (b). This behavior is expected for the dipole resonance associated with a simple bar resonator geometry as shown in Fig. 2.1. This is in good agreement with linearly polarized reflectance data reported by Braun and Maier [10]. A similar

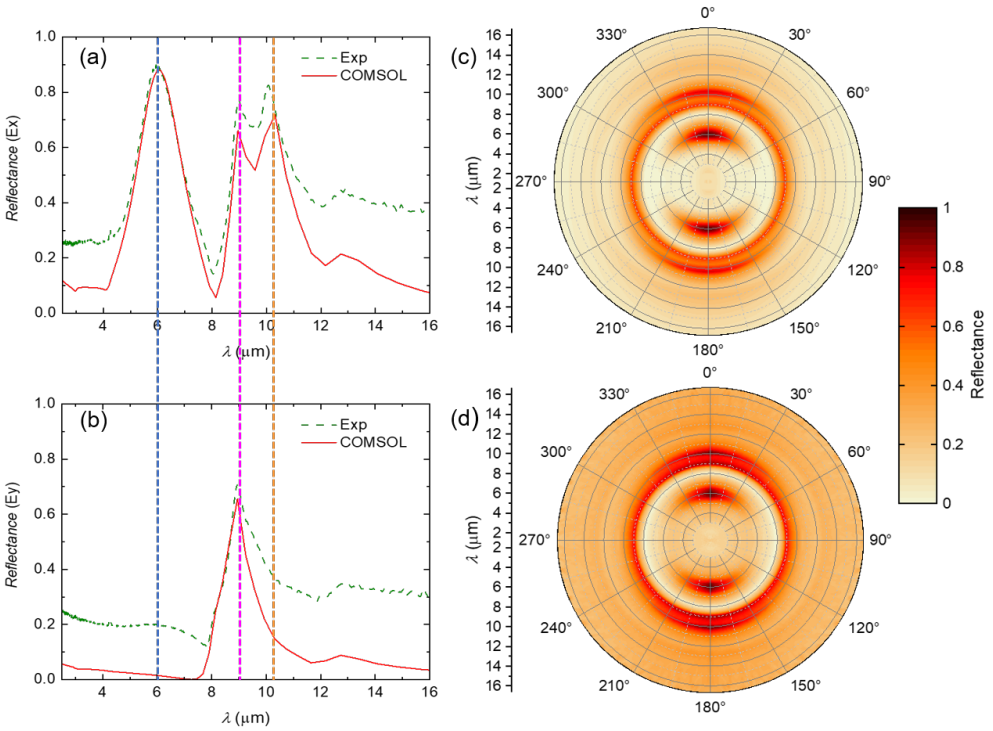

Figure 2.5: The measured (green dashed) and experimental (red solid) reflectance data for, linear polarization parallel to the long and short axis, is shown in panel (a) and (b), respectively. The dashed vertical lines from left to right indicate the position of the dipole resonance (blue), phonon resonance of the substrate (magenta), and the coupled dipole-phonon resonance (orange). Panels (c) and (d) depict a polar map of the simulated and experimental reflectance, respectively. The incident radiation is linearly polarized along the long axis of the bar resonator when the polarizer is oriented at 0°.

behavior can be observed for a resonance located at a wavelength of approximately 10.2 µm. For the resonance located at 9 µm the polarization sensitivity is lacking. This resonance is attributed to a phonon excitation in the silica substrate [19].

Panels (c) and (d) of Fig. 2.5 show the finite element model calculated and experimental polar maps of the polarized reflectance spectra, respectively. The polarization of the incident radiation is varied from 0° to 360° with a resolution of 1°. The azimuthal orientation of the polarization is denoted with respect to the long axis of the bar resonators. A polarization of 0° and 90° therefore corresponds to a polarization state parallel and perpendicular to the long axis of the resonator, respectively.

At a first glance a good agreement between the experimental and the model calculated data can be recognized. The most notable feature is the dipole resonance, which can be clearly observed at 6 µm with peaks in reflectivity at 0° and 180° in Fig. 2.5 (c) and (d). The polarization behavior of the second polarization dependent resonance at 10.2 µm is also well reproduced. We attribute this resonance to a coupling between the phonon resonance and dipole resonance of the metasurface. Such coupling phenomena have recently attracted much attention, but are outside of the scope of this work. The interested reader is referred to Ref. [9, 20, 21] and references therein. At 9 µm the polarization independent phonon resonance of the silica substrate can be observed in both panels.

2.5 Conclusion

We have demonstrated the fabrication of metasurfaces for the infrared spectral range using a three-step process which includes the maskless deposition of a patterned sacrificial layer by two-photon polymerization. A simple metasurface composed of bar resonators arranged on the surface in a square unit cell was used to demonstrate the capabilities of this synthesis approach. The fabricated metasurfaces exhibit features with as-designed dimensions and high structural fidelity.

A comprehensive infrared-optical characterization using polarization-sensitive reflection measurements was carried out. We found a good agreement between the experimental reflection data and the model-based calculated reflection data. Several reflectance maxima were identified in the spectral range from 2 µm to 16 µm. One resonance with a distinctive polarization characteristic was attributed to the dipole resonance of the bar resonator. In addition, we identified a resonance in the vicinity of the polarization independent substrate phonon-resonance which exhibits a similar polarization dependence as the dipole resonance. Such coupled excitations between dipole and substrate phonon resonances have been observed for several substrate materials in the infrared spectral range, but so far have not been presented for fused

silica.

In summary, we have shown that direct laser writing allows the maskless fabrication of 2D metasurfaces with high structural fidelity. State-of-the-art direct laser writing systems provide voxel sizes which enable the printing of patterned sacrificial layers with geometries optimized for the infrared spectral range. The maskless, direct laser writing-based, process presented here therefore provides a suitable alternative for cost-effective, rapid prototyping of metasurfaces. In contrast to classical fabrication of metasurfaces, the complex and time consuming fabrication of lithographic masks is completely omitted. We envision that this technique will provide a suitable fabrication approach for rapid prototyping and cost-effective manufacturing of infrared plasmonic metasurfaces with complex geometries and applications in areas such as perfect absorption and index sensing.

REFERENCES

[1] R. Walser, "Complex mediums II: beyond linear isotropic dielectrics," *Complex Mediums II: Beyond Linear Isotropic Dielectrics*, pp. 1–15 (2001).

[2] A. K. Sarychev and V. M. Shalaev, "*Electrodynamics of Metamaterials*," World Scientific (2007).

[3] M. Zhang, M. Pu, F. Zhang, Y. Guo, Q. He, X. Ma, Y. Huang, X. Li, H. Yu, and X. Luo, "Plasmonic metasurfaces for switchable photonic spin–orbit interactions based on phase change materials," *Adv. Sci.* **5**, p. 180083 (2018).

[4] Y.-X. Peng, K.-J. Wang, M.-D. He, J.-H. Luo, X.-M. Zhang, J.-B. Li, S.-H. Tan, J.-Q. Liu, W.-D. Hu, and X. Chen, "Electromagnetic near-field coupling induced polarization conversion and asymmetric transmission in plasmonic metasurfaces," *Opt. Commun.* **412**, pp. 1-6 (2018).

[5] M.-L. Wan, X.-J. Sun, Y.-L. Song, P.-F. Ji, X.-P. Zhang, P. Ding, and J.-N. He, "Broadband plasmon-induced transparency in plasmonic metasurfaces based on bright-dark-bright mode coupling," *Plasmon.* **12**, pp. 1555-1560 (2017).

[6] J. Hering, M. Eifler, L. Hofherr, C. Ziegler, J. Seewig, and G. von Freymann, "Two-photon laser lithography in optical metrology," *Advanced Fabrication Technologies for Micro/Nano Optics and Photonics XI*, **10544**, p. 1054412 (2018).

[7] A. Alipour, A. Farmani, and A. Mir, "High sensitivity and tunable nanoscale sensor based on plasmon-induced transparency in plasmonic metasurface," *IEEE Sens. J.* **18**, pp. 7047-7054 (2018).

[8] W. Wang, M. Ramezani, A. I. Väkeväinen, P. Törmä, J. G. Rivas, and T. W.

Odom, "The rich photonic world of plasmonic nanoparticle arrays," *Mater. Today* **21**, pp. 303-314 (2018).

[9] J. Kim, A. Dutta, G. V. Naik, A. J. Giles, F. J. Bezares, C. T. Ellis, J. G. Tischler, A. M. Mahmoud, H. Caglayan, O. J. Glembocki, A. V.Kildishev, J. D. Caldwell, A. Boltasseva, and N. Engheta, "Role of epsilon-near-zero substrates in the optical response of plasmonic antennas," *Opt.* **3**, pp. 339-346 (2016).

[10] A. Braun and S. A. Maier, "Versatile direct laser writing lithography technique for surface enhanced infrared spectroscopy sensors," *ACS Sens.* **1**, pp. 1155-1162 (2016).

[11] D. Wu, Y. Liu, R. Li, L. Chen, R. Ma, C. Liu, and H. Ye, "Infrared perfect ultra-narrow band absorber as plasmonic sensor," *Nanoscale Res. Lett.* **11**, pp. 1-9 (2016).

[12] M. N. Julian, C. Williams, S. Borg, S. Bartram, and H. J. Kim, "Reversible optical tuning of GeSbTe phase-change metasurface spectral filters for mid-wave infrared imaging," *Opt.* **26**, pp. 746-754 (2020).

[13] V.-C. Su, C. H. Chu, G. Sun, and D. P. Tsai, "Advances in optical metasurfaces: fabrication and applications," *Opt. Express* **26**, pp. 13148-13182 (2018).

[14] P. Genevet, F. Capasso, F. Aieta, M. Khorasaninejad, and R. Devlin, "Recent advances in planar optics: from plasmonic to dielectric metasurfaces," *Opt.* **4**, pp. 139-152 (2017).

[15] J. A. Kim, D. J. Wales, A. J. Thompson, and G.-Z. Yang, "Towards development of fiber optic surface enhanced raman spectroscopy probes using 2-photon polymerization for rapid detection of bacteria," *Plasmonics in Biology and Medicine XVI*, **10894**, p. 108940F (2019). SPIE.

[16] Y. Li, S. Park, M. McLamb, M. Lata, D. Childers, and T. Hofmann, "Fabrication of optical components with nm-to mm-scale critical features using three-dimensional direct laser writing," *2019 IEEE 16th International Conference on Smart Cities: Improving Quality of Life Using ICT & IoT and AI (HONET-ICT)*, pp. 213–216 (2019). IEEE.

[17] Y. Li, S. Park, D. B. Fullager, D. Childers, M. K. Poutous, I. D. Aggarwal, G. Boreman, and T. Hofmann, "Near-infrared transmittance enhancement using fully conformal antireflective structured surfaces on microlenses fabricated by direct laser writing," *Opt. Eng.* **58**, p. 010501 (2019).

[18] Y. Li, D. Fullager, E. Angelbello, D. Childers, G. Boreman, and T. Hofmann, "Broadband near-infrared antireflection coatings fabricated by three-dimensional direct laser writing," *Opt. Lett.* **43**, pp. 239-242 (2018).

[19] J. Luo, N. J. Smith, C. G. Pantano, and S. H. Kim, "Complex refractive index of silica, silicate, borosilicate, and boroaluminosilicate glasses–Analysis of glass network vibration modes with specular-reflection IR spectroscopy," *J. Non-Cryst. Solids*, **494**, pp. 94-103 (2018).

[20] R. Pollard, A. Murphy, W. Hendren, P. Evans, R. Atkinson, G. Wurtz, A. Zayats, and V. A. Podolskiy, "Optical nonlocalities and additional waves in epsilon-near-zero metamaterials," *Phys. Rev. Lett.* **102**, p. 127405 (2009).

[21] Y. C. Jun, J. Reno, T. Ribaudo, E. Shaner, J.-J. Greffet, S. Vassant, F. Marquier, M. Sinclair, and I. Brener, "Epsilon-near-zero strong coupling in metamaterial-semiconductor hybrid structures," *Nano Letters* **13**, pp. 5391-5396 (2013).

CHAPTER 3: Bi-encoded metasurfaces

3.1 Overview

Plasmonic metasurfaces composed of arrays of rectangular metallic bars are well known for their strong optical response in the infrared spectral range.[1] In this study, we explore the polarization sensitivity of plasmonic metasurfaces for encoding information. The polarization-sensitive optical response depends strongly on the orientation of the metallic bars allowing the encoding of information into the metasurface. Here we demonstrate that a 2-dimensional polarization encoded metasurface can be obtained by using mask-less two-photon polymerization techniques. This novel approach for the fabrication of plasmonic metasurfaces enables the rapid prototyping and adaptation of polarization sensitive metasurfaces for the encoding of multiplexed images.

3.2 Introduction

Metamaterials describe a group of materials with properties that are not typically found in nature. Metamaterials are designed to manipulate phase, amplitude, and polarization of electromagnetic radiation by implementing an array of subwavelength components with arbitrary optical properties which eliminates the need for classically bulky optical systems [1]. Metasurfaces are a subset of metamaterials which eliminate the height dimension of metamaterials in favor of a simpler design permitting an easing of the precision of fabrication requirements. Plasmonic metasurfaces are composed of a metallic array of components that utilize the plasmonic resonances, known

[1]Reprinted by permission from SPIE M. McLamb, Y. Li, V. P. Stinson, N. Shuchi, D. Louisos and T. Hofmann, "Bi-encoded metasurfaces for the infrared spectral range," *Optical Components and Materials XX* **12417**, 101-105 (2023).

as surface plasmon polaritons, to manipulate the optical response of incoming electromagnetic radiation and have a wide field of applications[1, 2, 3]. A few examples of metasurface applications include beam steering, planar metalenses, holography, and narrow and broadband absorbers[1, 2, 4, 5]. Metasurfaces can be fabricated using many techniques, for example, electron beam lithography, focused ion beam milling, interference lithography, and nano-imprint lithography, to name a few. Two-photon polymerization has been established as a mask-less lithographic technique which allows the fabrication of metasurfaces [6, 7].

This work aims to show proof of concept for the encoding of information into a plasmonic metasurface fabricated using two-photon polymerization techniques. A metasurface composed of an arrangement of rectangular dipoles on a dielectric surface was designed and fabricated using two-photon polymerization with subsequent metallization. The metasurface was intended for use in the infrared spectrum. The reflected amplitude varies as a function of the linear polarization profile of the incident radiation to produce two distinct images. In this case, the image created by aligning the linear polarization along $0° + (n{\cdot}180°)$ of the dipole resonator produces the image of a "1" and aligning the linear polarization in angles of $45° + (n{\cdot}90°)$ forms the image of a "0" (where $n = 0,\ 1,\ 2, ...$). The fabrication of the metasurface uses a three-step technique that involves two-photon polymerization on a dielectric slap subsequently followed by a metallization step using electron-beam evaporation to form the metallic layer. The polymerized layer is then removed post-metallization with a lift-off technique leaving only the metallic dipoles on the dielectric layer. The encoding of metasurfaces through the polarization profile of incident radiation has applications in color display, information security, and anti-counterfeiting [3]. This work will discuss the basic design principles, fabrication process, and experimental results for the rapid prototyping of an encoded polarization sensitive plasmonic metasurface.

3.3 Design and Fabrication

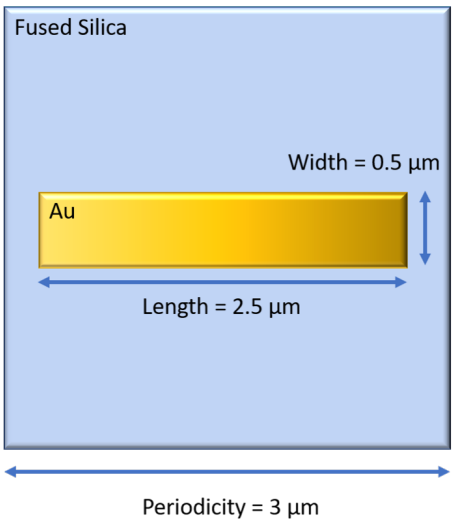

Figure 3.1: Represents the unit cell used in COMSOL Multiphysics. The bar resonator is composed of Au with 38 nm thickness which rests on a slab of fused silica with a square periodicity of 3 µm. The length and width of the bar resonator is 2.5 µm and 0.5 µm respectively.

The dimensions and arrangement for the bar resonators were determined using finite element modeling (COMSOL). The resonators are arranged in a square lattice. The COMSOL calculations further require accurate knowledge of the constituents of the metasurface. The dielectric function of the fused silica substrate (Nanoscribe GmbH) was determined through spectroscopic ellipsometry in the range from 2 µm - 33 µm (IR-Vase, J.A. Woollam Co., Inc.). [6]. The Au optical properties are modeled with a single Drude oscillator with parameters $\rho_1 = (3.3 \pm 3 \times 10^{-7}) \times 10^{-6}$ Ω/cm, $\tau_1 = (18 \pm 1.13)$ fs. The boundaries of the unit cell were given periodic conditions to simulate an infinite array of resonators. The dimensional parameters of the unit cell were varied in order to determine the optimal conditions for a resonance to occur at a wavelength 6 µm when normally incident radiation is linearly polarized along the long axis and no resonance when polarized along the short axis of the resonator. The thickness of the Au layer was controlled at 38 nm, consistent with the measured

thickness of the Au witness sample, with fused silica as the substrate, measured with spectroscopic ellipsometry. The optimal dimensions for a central reflectance maximum at $\lambda = 6$ µm were found to be $l = 2.5$ µm, $w = 0.5$ µm, and $p = 3$ µm. The unit cell can be viewed in Fig. 5.1. The results of the simulation were verified with experimental results which can be viewed in a previous publication [6]. For brevity, the results of the simulation and experiment can be seen in Fig. 3.2. The reflectance map is used to determine what orientations should be used to create two distinct images. The green dots in Fig. 3.2 represent polarization states where the image of a "1" will appear, conversely, the red dots indicate states where the image of a "0" will appear. There is a secondary reflectance that is apparent at $\lambda = 9$ µm which arises due to vibrational mode within the fused silica substrate.[8] This reflectance maximum can be observed in all cases and thus can be determined to be polarization insensitive.

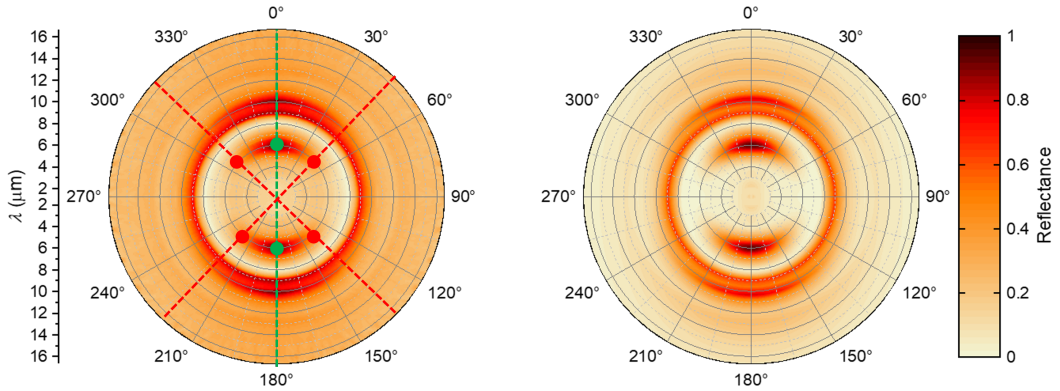

Figure 3.2: Polar plot of the reflectance of the dipole array as a function of the input polarization. A reflectance maximum appears at 0° and 180°. These angles are marked by a green dot signaling the "on" state of the metasurface. As the orientation of the polarization profile shifts the reflection maximum begins to decrease. At iterations on $45° + n \cdot 90°$ the metasurface is considered to be in the "off" state marked by a red dot.

Once the optimal dimensions were determined, the resonators must be oriented

in such a way as to construct an image when illuminated with the appropriate polarization. This was done by digitizing images of a "1" and "0" with pixels set at a periodicity of 3 µm using Matlab. Each image has two possible combinations, either "on" or "off" meaning there are four distinct combinations of images. These four sets of coordinates are superimposed on each other to create the locations and orientations of the bar resonators which can be seen in Fig. 3.3.

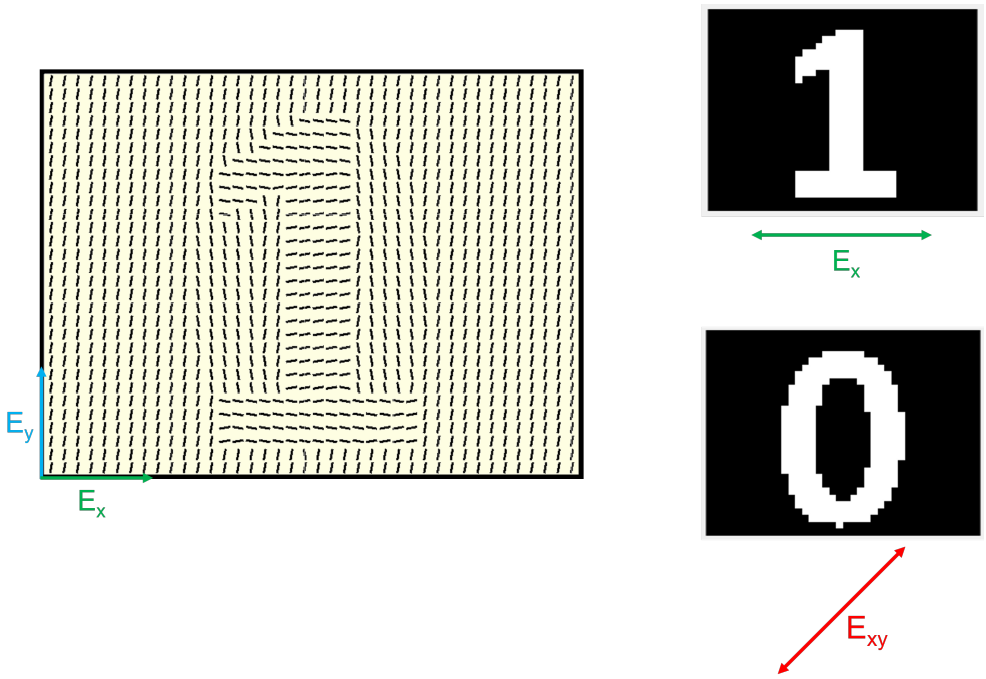

Figure 3.3: Displays the schematic of the location and orientation of metallic bars for the encoded metasurface. The panels on the right display the image corresponding with the polarization of the incident electric field. When the incident radiation is polarized in $\hat{x}$ the metasurface will appear in the image of a "1." When the incident radiation is polarized in $\hat{xy}$ the metasurface results in the image of a "0."

The total image coordinates obtained in Matlab are used to create a write file of the inverse of the desired metasurface which is fabricated by a commercial two-photon lithography system (Nanoscribe GmbH). The inverse pattern is constructed on a $25\times25\times0.75$ mm^3 slide of fused silica. The fused silica substrate is prepared prior to deposition by rinsing with isopropanol-2 and drying with N_2. IP-Dip was used to

fabricate a 200 µm thick inverse geometry sacrificial layer. After polymerization the excess monomer is rinsed from the sample using propylene glycol monomethyl ether acetate and isopropanol-2 for two minutes and 5 minutes respectively. Once the excess monomer is removed the sample is allowed to air dry at room temperature for five minutes [6].

After the direct laser writing of the patterned sacrificial layer is completed, the sample was metallized (Kurt J. Lesker PVD 75). Initially, electron-beam evaporation was used to deposit a 7 nm adhesion layer of chromium, sourced from chromium pieces (99.95%) and, immediately following, a 38 nm Au layer (determined experimentally using spectroscopic ellipsometry) evaporated from Au pellets (99.99%). Both films were deposited at a rate of 1 Å/s. All depositions were carried out at room temperature at a pressure of 2.53 Pa. The substrate holder was rotated during the deposition at approximately 15 rpm to ensure a homogeneous film thickness across the entire sample [6].

After the metallization, the sacrificial photoresist layer was removed by plasma cleaning at 150 W and a 12 SCCM flow of O_2 (Tergeo Plus, Pie Scientific). After the plasma cleaning, the substrate is completely immersed in acetone until the sacrificial photoresist layer is lifted off completely. Subsequently, the sample is cleaned by rinsing with isopropanol-2 and methanol and dried with N_2 [6].

3.4 Results and discussion

Linearly polarized reflectance data was captured using a Hyperion 3000 microscope (Bruker) in combination with a Vertex 70 FTIR spectrometer (Bruker) though a 90×90 µm^2 square aperture. The reflectance measurements were captured at 11° angle of incidence using a 15x IR Schwarzschild objective with confocal illumination [9]. A mercury cadmium telluride focal plane array detector was used for all measurements. An adjustable, KRS-5, wire-grid polarizer mounted in a custom-built, electro-mechanical, rotation stage was used to polarize the incident radiation.

The results of the hyperspectral imaging can be seen in Fig. 3.4. The image on the left was taken with an optical microscope to inspect the fidelity of the metasurface post lift-off. Compared to the schematic shown in Fig. 3.3 a good conformity with the as designed geometry can be observed. The panels to the right of the microscope image depict the hyperspectral images given their corresponding polarizations. When the electric field is polarized in $\hat{x}$ the metasurface displays a "1" and contrarily when polarization is in $\hat{xy}$ the metasurface yields the image of a "0." It can be seen in the polarized reflectance legend that the "1" and "0" reach nearly full reflectance while the surrounding resonators are either much lower, in the case of the "1," or slightly lower, in the case of the "0." This difference in reflectance provides the necessary contrast to observe the definite image. The image is acquired at the wavelength of 6 µm and the vibrational mode of the fused silica substrate does not affect the image quality.

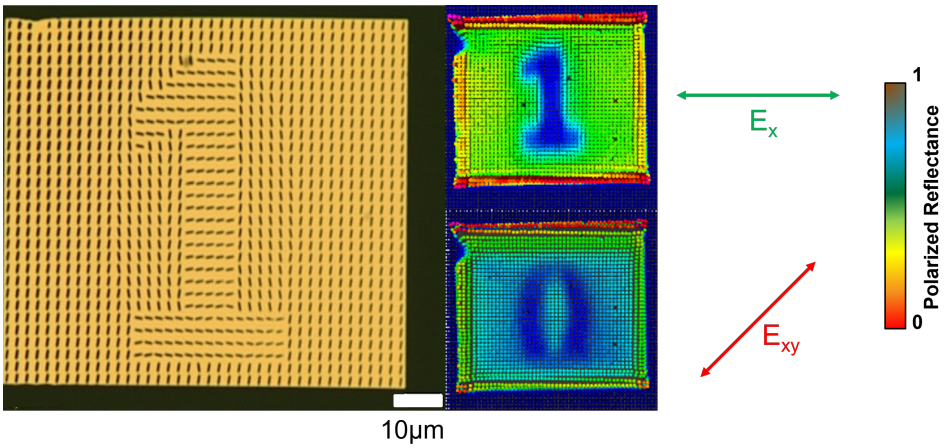

Figure 3.4: An optical microscope image taken in transmission mode of the metasurface post fabrication to determine the fidelity of the metasurface. The panels to the right of the microscope image depict hyperspectral images obtained at $\lambda = 6$ µm when illuminated with linear polarization in $\hat{x}$ and $\hat{xy}$ corresponding to the image of a "1" and "0" respectively.

3.5 Conclusion

A plasmonic metasurface was designed and fabricated for the infrared spectral range that allows for the encoding of images. For this particular metasurface two

distinct images are encoded, a “1” and a “0.” The fabrication of this metasurface uses a three step process, the direct laser writing of an inverse sacrificial layer using two-photon polymerization, a metallization step using electron-beam evaporation, and then the removal of the patterned sacrificial layer using a lift-off procedure [6]. The fabricated metasurface was characterized using hyperspectral imaging to determine the quality of the encoded images. The measurements displayed distinct depictions of the encoded information with sufficient contrast to discern profile and background. This metasurface serves as a proof of concept for applications such as color display, information security, and anti-counterfeiting in the infrared region.

REFERENCES

[1] F. Ding, "A review of multifunctional optical gap-surface plasmon metasurfaces," *Pr. Electromagn. Res. S.* **174**, pp. 55–73, (2022).

[2] A. C. Tasolamprou, E. Skoulas, G. Perrakis, M. Vlahou, Z. Viskadourakis, E. N. Economou, M. Kafesaki, G. Kenanakis, and E. Stratakis, "Highly ordered laser imprinted plasmonic metasurfaces for polarization sensitive perfect absorption," *Sci. Rep.-UK* **12**, p. 19769, (2022).

[3] F. Dong and W. Chu, "Multichannel-independent information encoding with optical metasurfaces," *Adv. Mater.* **31**, p. 1804921, (2018).

[4] J. Wang and J. Du, "Plasmonic and dielectric metasurfaces: Design fabrication and applications," *Appl. Sci.* **6**, p. 239, (2016).

[5] X. Zang, F. Dong, F. Yue, C. Zhang, L. Xu, Z. Song, M. Chen, P.-Y. Chen, G. S. Buller, Y. Zhu, S. Zhuang, W. Chu, S. Zhang, and X. Chen, "Polarization encoded color image embedded in a dielectric metasurface," *Adv. Mater.* **30**, p. 1707499, (2018).

[6] M. McLamb, Y. Li, P. Stinson, and T. Hofmann, "Metasurfaces for the infrared spectral range fabricated using two-photon polymerization," *Thin Solid Films* **721**, p. 138548, (2021).

[7] M. McLamb, S. Park, V. P. Stinson, Y. Li, N. Shuchi, G. D. Boreman, and T. Hofmann, "Tuning of reciprocal plasmonic metasurface resonances by ultrathin conformal coatings," *Optics* **3**, pp. 70–78, (2022).

[8] J. Luo, N. J. Smith, C. G. Pantano, and S. H. Kim, "Complex refractive index of silica, silicate, borosilicate, and boroaluminosilicate glasses â analysis of glass

network vibration modes with specular-reflection ir spectroscopy," *J. Non-Cryst. Solids* **494**, pp. 94–103, (2018).

[9] V. P. Stinson, S. Park, M. M, G. Boreman, and T. Hofmann, "Photonic crystals with a defect fabricated by two-photon polymerization for the infrared spectral range," *Optics* **2**, pp. 284–291, (2021).

CHAPTER 4: Theoretical study of enhanced plasmonic-photonic hyrbrid cavity modes in reciprocal plasmonic metasurfaces

4.1 Overview

A new configuration for metasurface construction is presented to exhibit potential multi-functionalities including perfect absorption, bio/chem sensing, and enhancement of light-matter interaction.[1] The reciprocal plasmonic metasurfaces discussed here are composed of two plasmonic surfaces of reciprocal geometries separated by a dielectric spacer. Compared to conventional metasurfaces this simple geometry exhibits an enhanced optical performance due to the hybrid plasmonic-photonic cavity. The discussed reciprocal metasurface design further enables effective structural optimization and allows for a simple and scalable fabrication. The physical principle and potential applications of the reciprocal plasmonic metasurfaces are demonstrated using numerical and analytical approaches.

4.2 Introduction

Metasurfaces are resonant textured surfaces with unit cells much smaller than the wavelength of incident electromagnetic radiation [1]. One of the most frequently used metasurface designs are heterostructures composed of triple-layered constituents which are optimized for optical frequencies [2, 3, 4, 5, 6, 7, 8, 9, 10]. Such heterostructured metasurfaces have been extensively studied over the past decade and exhibit excellent optical performance [11, 12, 13, 14, 15, 16, 17, 18, 19, 20, 21].

Despite these advances, the explored designs often require complex nanofabrication

[1]Reprinted by permission from Springer Nature Customer Service Centre GmbH: Springer Y. Li, M. McLamb, S. Park, D. Childers, G. D. Boreman and T. Hofmann, "Theoretical Study of Enhanced Plasmonic-Photonic Hybrid Cavity Modes in Reciprocal Plasmonic Metasurfaces," *Plasmonics* **16**, 2241-2247 (2021).

processes which can lead to a reduced performance of the as-synthesized metasurfaces compared to numerical results obtained from optimized, nominal designs [22]. For example, one of the most common fabrication defects when using a mask or lift-off processes is the dislocation of elements of the metasurface [23, 22]. Furthermore, loss in fidelity often results in an imperfect reproduction of the nominal geometries of the metasurfaces constituents [23, 22, 24]. These imperfections directly impact the performance of the heterostructured metasurfaces. For instance, in metasurfaces designed as perfect absorbers, the experimentally observed absorption values are often much lower [23]. In addition, fabrication-induced imperfections can lead to grain boundaries between areas with different defect densities, which can further diminish the performance of the entire metasurface [22].

Here we introduce a metasurface design that can be synthesized using a simple two-step fabrication process. The process envisioned here consists of the deposition of a structured polymer layer and a subsequent metallization. This results in two metal-based metasurfaces with reciprocal geometry separated by a dielectric spacer, forming a plasmonic-photonic cavity. The reciprocal plasmonic metasurface with its hybrid cavity mode is theoretically studied here using finite-element-based numerical and analytical effective medium optical models. It is found that reciprocal plasmonic metasurface designs exhibit the potential for applications in perfect absorption, sensing of minute ambient refractive index changes, and enhancement of spontaneous emission, compared to conventional heterostructured metasurfaces. The record values obtained for the figure of merit for refractive index sensing suggest that these structures are ideal candidates for extremely sensitive ambient index sensors [4]. In addition to providing enhanced optical performance, the reciprocal plasmonic metasurface discussed here dramatically reduces the fabrication complexity compared to the currently existing heterostructured metamaterials.

4.3 Design and Theoretical Models

The geometry of this reciprocal metasurface is depicted in Fig. 4.1. The top plasmonic metasurface is composed of rectangular bars while the bottom metasurface has a reciprocal arrangement with rectangular openings in a metallized surface. The dielectric spacer is formed by fins with a rectangular base.

The optical performance of the reciprocal metasurface is optimized by carefully engineering the geometrical parameters using a numerical optical model based on the finite-element method (FEM, COMSOL® 5.3) as shown in Fig 4.2. The reciprocal metasurface was developed to achieve a narrow and strong absorption at a wavelength of 1.55 µm and a quality factor of 20, which is relevant for telecommunication applications. In addition, the physical mechanism of the reciprocal metasurface has been theoretically studied by an effective medium optical model based on interference theory [25], as shown in Fig. 4.3.

The reciprocal metasurface designed here consists of a dielectric fin-array sandwiched by two Au patterned layers, as shown in Fig. 4.1. This array is composed of fins with the following dimensions: length L=0.9 µm, width W=0.3 µm, periodicity P=1 µm, and height H=1.25 µm in a square lattice pattern, as shown in Fig. 4.1 (c). This design allows rapid prototyping for instance using two-photon polymerization and while the simplicity of the geometry enables the fabrication of larger surface areas using standard lithography techniques [26]. For the calculations discussed below, it was assumed that the top bar resonator array and bottom perforated film are fabricated from Au with a thickness of 50 nm. The dielectric spacer is assumed to be composed of IP-Dip, a polymer compatible with the two-photon polymerization process, for which the optical properties are well known in the infrared and visible spectral range [27].

Fig. 4.2 (a) shows the calculated reflectance spectrum (black solid line) of the optimized reciprocal metasurface under normal incidence illumination with the plane

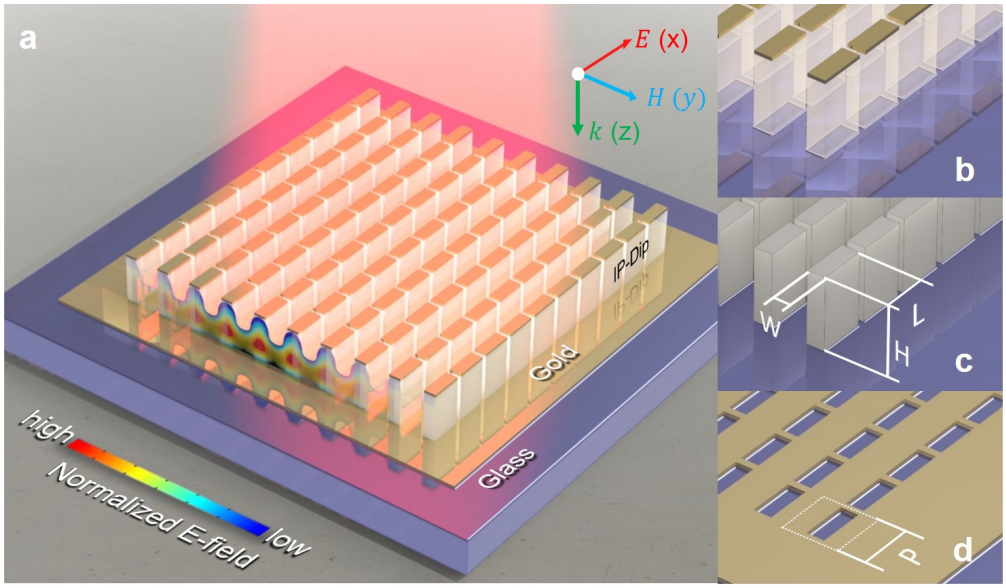

Figure 4.1: (a) The reciprocal metasurface composed of a three-layered heterostructure: Au bar-antenna array (b), polymer-based fin-array (c), and a patterned Au surface reciprocal to the rectangular bar array (d).

electric field polarized along the long axis of the bars (x-axis). Note that in the simulation periodic boundary condition was applied to the four side faces of the unit cell. Two perfectly matched layers were employed on the top and at the bottom of the unit cell to optimize the simulation with open boundaries along vertical direction. In the spectral range from 1.3 µm to 3.5 µm, two nearly-zero-valued minima centered at 1.55 µm and 2.70 µm can be observed.

For comparison, the response of the top metasurface (rectangular bar array, orange solid line) and the bottom metasurface (rectangular hole array, red solid line) are also depicted in Fig. 4.2 (a).

The normalized electric and magnetic field distributions $|\vec{E}|$ and $|\vec{H}|$, respectively, corresponding to the two resonant wavelengths are shown in Fig. 4.2 (c) - (h), respectively. The field distributions for H=1.25 µm in Fig. 4.2 (c) - (e) and (f) - (h) depict a second-order harmonic and fundamental harmonic standing wave for the wavelengths of 1.55 µm and 2.70 µm, respectively. The locations of the reflectance minima depend linearly on the the cavity height H. This is illustrated in the reflectance map shown

in Fig. 4.2 (b) where the reflectance is plotted as a function of H valued from 0.5 µm to 1.7 µm over the spectral range from 1.3 µm to 3.5 µm. Fig. 4.2 (b) also indicates an additional higher-order mode, which can be accessed if the dielectric fin-array has a sufficient height. For the investigated spectral range, higher-order modes can be observed for H>0.9 µm. It can be concluded that with increasing H, the resonant modes of the reciprocal metasurface red-shift while higher-order modes start to appear at the short wavelength end of the spectrum.

In addition to being a function of the cavity height H, the optical response of the reciprocal metasurface also depends on the plasmon resonance of the Au bar-antenna array. The reflectance (orange solid line) and transmittance (orange dotted line) spectra of the top Au bar-antenna array are included in Fig. 4.2 (a) for comparison indicating a plasmon resonance at 2.07 µm. Note, that the modes of the reciprocal metasurface are interrupted in the vicinity of the plasmon resonance as can be clearly seen in the reflectance map Fig. 4.2 (b). This is due to the lack of transparency of the top metasurface as shown in Fig. 4.2 (a) which prevents the effective coupling to the bottom metasurface.

The reflectance of perforated Au film at the bottom of the reciprocal metasurface (red solid line, Fig. 4.2 (a)), on the other hand, shows very little variation as a function of the wavelength. This observation is relevant for the development of an analytical model discussed below where the perforated Au film at the bottom of the reciprocal metasurfaces is treated as a plasmonic mirror reflecting all the wavelengths of interest.

Based on the results of the FEM-based calculations, an analytical effective medium-based formalism is developed in the following. In contrast to the FEM-based numerical model the analytical model allows the rapid determination of the geometry parameters of the reciprocal metasurface which are required to obtain specific target frequencies for its absorption bands. In addition, this model further provides insights into the physical mechanism which is driving the plasmonic-photonic hybrid cavity

modes of the reciprocal metasurfaces discussed here.

Figure 4.3 (a) depicts the concept of the effective medium optical model. Due to the sub-wavelength-sized structural features of the dielectric fin-array [as shown in Fig. 4.1 (c)], it can be treated as a single layer with an effective index n_{eff}. n_{eff} can be calculated using the Bruggeman effective medium approximation and the complex dielectric function of the constituent material IP-Dip [26, 28, 29]. This layer is enclosed by two reflective surfaces (top Au bar array and bottom Au perforated film) which are denoted in Fig. 4.3 (a) as top and bottom mirror.

As the incident electromagnetic radiation transmits through the top partially transparent mirror [Fig. 4.3 (a)], a cavity mode forms inside the effective medium layer. This phenomenon only occurs when these waves oscillate in phase, i.e., the phase difference $\Delta\varphi$ after a round trip are integer multiples of 2π:

$$\Delta\varphi = \varphi_{\text{t}} + \varphi_{\text{b}} + \varphi_{\text{prop}} = N2\pi \quad (N = 1, 2, ...), \tag{4.1}$$

where φ_{t} and φ_{b} respectively denote the phase changes induced by the interaction of the electrical radiation with the top and bottom mirrors, for which the numerical calculations on each individual part determine their spectra shown in Fig. 4.3 (b). The phase change due to the propagation in the effective medium φ_{prop} is calculated by $\varphi_{\text{prop}} = 2\pi H n_{\text{eff}}/\lambda$ for $H = 1.25$ μm and also included in Fig. 4.3 (b) (black solid line).

Varying the value of the cavity height H in the same range as the one used in the numerical simulation shown in Fig. 4.2 (b), Eqn. (4.1) allows the identification of the cavity resonances with $N = 1$, 2, and 3 which are depicted by the black dotted lines in Fig. 4.3 (c). Note, that the results for the reflectance map of the FEM-based model [Fig. 4.2 (b)] are reproduced here again for direct comparison.

A good agreement between the analytically calculated and the numerically simulated results is achieved for the location of the reciprocal metasurface modes. This

confirms the optical-cavity-based mechanism of the reciprocal metasurface.

The reflectance map [Figs. 4.2 (b) and 4.3 (c)] further revealed that the strength of the cavity modes are wavelength dependent, an effect which can not be obtained using a simple phase analysis as shown in Eqn. (4.1). Instead, this effect can be described considering the relative amplitude $|E_{\mathrm{cav}}|$ of an infinite number of electric fields that constructively interfere inside the layer with the effective index n_{eff}:

$$|E_{\mathrm{cav}}| \propto \frac{t_{\mathrm{t}}^2}{1 + |r_{\mathrm{t}}^2 r_{\mathrm{b}}^2|}, \tag{4.2}$$

where t_{t},r_{t}, and r_{b} denote the transmissivity and reflectivity for the top and bottom mirrors, respectively, and their values are derived from the corresponding transmittance and reflectance spectra obtained by the FEM-based calculations [Fig. 4.2 (a)].

$|E_{\mathrm{cav}}|$ is shown in Fig. 4.3 (d) for the spectral range from 1.3 to 3.5 µm. Two maxima centered at 1.60 µm and 2.66 µm can be observed. The minimum at 2.07 µm corresponds to the plasmon resonance of the top mirror. The pair of the plasmonic surfaces therefore influence the phase change at both interfaces and modulate the electromagnetic field amplitude inside the cavity, consequently, the resonance frequency and its amplitude can be tuned by changing the geometry of the plasmonic surfaces and the cavity height H.

Additionally, the interference-based optical model can be validated using the numerically calculated dispersion relation as shown in Fig. 4.4. The inset of Fig. 4.4 describes two incident conditions: 1) Transverse magnetic field is incident at an angle θ_x ranging from 0° to 16° in x-z plane, and 2) transverse electric field is incident at angle θ_y of the same angular range in y-z plane. The angle of incidence-dependent reflectance maps corresponding to the two incident conditions are depicted in the left and right half of the figure, where the black areas represent the reflectance minima. With increasing the angle of incidence, the cavity modes are nearly invariant for both incident conditions, meaning a zero-valued group velocity in z-direction. The

angle-resolved reflectance maps therefore corroborate the character of standing wave supported in the plasmonic cavity along z-direction, of which the typical electric field distributions inside the plasmonic cavity are instructively represented as shadowed profiles in Fig. 4.2 (d) and (g).

A comprehensive understanding of the optical mechanism of the reciprocal metasurface has been achieved. In the following section, potential applications of the designed metasurface are briefly explored.

4.4 Discussion and Applications

Fig. 4.5 (a) depicts the absorption spectrum (red solid line) of the optimized reciprocal metasurface. Two absorption peaks at wavelength of 1.55 µm and 2.70 µm can be observed. The Q-factor for both absorption peaks is approximately 20. Therefore the reciprocal metasurface could be readily applied as a narrow-band perfect absorber in the near-infrared spectral range for which the absorption frequencies can be easily adjusted by the geometry and the refractive index of the dielectric spacer of the reciprocal metasurface.

Furthermore, this type of metasurface is an excellent candidate for sensing applications due to its high sensitivity to the ambient refractive index n, as shown in the inset of Fig. 4.5 (a). An index change of 0.01 would result in a shift of the resonant wavelength of 0.02 μm which can be easily detected. Its sensing capability is characterized in terms of sensitivity S^*, defined as the ratio of the intensity change vs. the change in refractive index, while the figure of merit FOM^* is the ratio of S^* vs. the absolute intensity [4]. For the example depicted in Fig. 4.5 (b) and (c) S^* is a approximately 18, while FOM^* is found to be larger than 8000. This extreme sensitivity is due to the strong change of the plasmonic resonance of the top and bottom metasurfaces upon ambient index variation. Furthermore, the effective refractive index of the cavity n_{eff} also varies as a function of the ambient refractive index, amplifies the changes in the optical response of the reciprocal metasurface.

In addition to the discussed applications for sensing and as a perfect absorber, the intense near field confinement is another critical characteristic of the reciprocal plasmonic metasurface that allows for the exploration of strong light-matter couplings, such as the plasmon-exciton polariton, spontaneous emission enhancement, and surface enhanced Raman spectroscopy (SERS). In Fig. 4.5 (d), assuming that a fluorescent material with refractive index n larger than or comparable to that of the polymer fins is integrated into the metasurface and fills up the space between the fins, a strongly localized electric field $\vec{E}$ approaching to 1.19×10^8 V/m can be observed between the fins while the amplitude of the source electric field is 1 V/m. It is worthy to note that in contrast to air as host medium, materials with large-valued refractive index can shift the local maximum of the electric field away from the polymer fins' area (see Fig. 4.2 (e) and (h)). This increases the interaction of the field of light with the materials to be measured. Given the partial transparency of the Au bar-antenna array that can serve as the top mirror of the cavity, it is encouraging to further study the reciprocal plasmonic metasurface for surface-mode lasing functionality by exploiting the enhancement effect.

4.5 Conclusion

To conclude, the optical properties of a reciprocal plasmonic metasurface were theoretically studied using a FEM-based approach and an effective medium optical model. The near-infrared optical response of the reciprocal metasurface discussed here reveals strong resonances for which almost perfect absorption is found, assuming realistic dielectric properties of the constituents. It is demonstrated that the hybrid resonance frequencies can be easily tuned by changing the height of the dielectric spacer between the top and bottom Au layers with reciprocal geometries.

The results of the FEM-based calculations are in very good agreement with the data obtained from the analytical, effective medium based model. In comparison with the FEM-based model, the analytical effective-medium-based optical model al-

lows the rapid optimization of the geometry of the reciprocal metasurface for a wide range of target frequencies. The analytical model further reveals the cause of the strong absorption peaks, which is an interplay between an effective optical-cavity and the plasmon resonances of the reciprocal top and bottom surfaces. On the basis of the developed theoretical model, the invariant dispersion relation of the metasurface exhibited in the specific incident angle range is clarified qualitatively in conjunction with the numerically simulated reflectance maps.

The theoretical findings presented here illustrate the advantages of the reciprocal plasmonic metasurfaces in the applications of perfect absorption. The narrow absorption characteristic and its strong dependence on the ambient refractive index further suggest that reciprocal metasurfaces can be employed as optical sensors. Because of the enhanced light-matter interaction arising from the reciprocal geometry, a higher sensitivity has been obtained compared to other metasurfaces engineered for ambient sensing [4, 17, 30, 31, 32, 33].

In addition to applications for perfect absorption and sensing of minute ambient refractive index changes, localized electric field calculations exhibit an enhancement effect which could be exploited to construct a novel plexciton platform for realizing strong light-matter coupling effects.

While studied theoretically here, reciprocal metasurfaces have substantial practical implications as the simplicity of its design suggests a considerable reduction in fabrication complexity often plaguing heterostructured metasurfaces demonstrated so far. In fact, the discussed geometry is suitable for a simple two-step fabrication. In the first step the dielectric spacer would be deposited, for instance using maskless two-photon polymerization approaches. In the subsequent metallization step the reciprocal top and bottom surfaces can be deposited at the same time.

We believe that the reciprocal plasmonic metasurfaces can open a new avenue for the design and fabrication of metasurfaces with enhanced performance yet low

manufacturing time and cost.

REFERENCES

[1] W. Cai and V. Shalaev, "*Optical Metamaterials: Fundamentals and Applications*," Springer Science & Business Media (2009).

[2] N. Landy, S. Sajuyigbe, J. J. Mock, D. R. Smith, and W. J. Padilla "Perfect metamaterial absorber," *Phys. Rev. Lett.* **100**, p. 207402 (2008).

[3] H. T. Chen, J. Zhou, J. F. O'Hara, F. Chen, A. K. Azad, and A. J. Taylor, "Antireflection coating using metamaterials and identification of its mechanism," *Phys. Rev. Lett.*, **105**, p. 073901 (2010).

[4] R. Ameling, L. Langguth, M. Hentschel, M. Mesch, P. V. Braun, and H. Giessen, "Cavity-enhanced localized plasmon resonance sensing," *Appl. Phys. Lett.* **97**, p. 253116 (2010).

[5] D. Y. Shchegolkov, A. Azad, J. O'hara, and E. Simakov, "Perfect subwavelength fishnetlike metamaterial-based film terahertz absorbers," *Phys. Rev. B* **82**, p. 205117 (2010).

[6] M. Pu, C. Hu, M. Wang, C. Huang, Z. Zhao, C. Wang, Q. Feng, and X. Luo, "Design principles for infrared wide-angle perfect absorber based on plasmonic structure," *Opt. Express* **19** pp. 17413-17420 (2011).

[7] A. Vázquez-Guardado, A. Safaei, S. Modak, D. Franklin, and D. Chanda, "Hybrid coupling mechanism in a system supporting high order diffraction, plasmonic, and cavity resonances," *Phys. Rev. Lett.* **113**, p. 263902 (2014).

[8] B. X. Wang, Y. He, P. Lou, and H. Zhu "Multi-band terahertz superabsorbers based on perforated square-patch metamaterials," *Nanoscale Adv.* **3**, pp. 455-462 (2021).

[9] B. X. Wang, Y. He, P. Lou, and W. Xing, "Design of a dual-band terahertz metamaterial absorber using two identical square patches for sensing application," *Nanoscale Adv.* **2**, pp. 763-769 (2020).

[10] B. X. Wang, C. Tang, Q. Niu, Y. He, and R. Chen, "A broadband terahertz metamaterial absorber enabled by the simple design of a rectangular-shaped resonator with an elongated slot," *Nanoscale Adv.* **1**, pp. 3621-3625 (2019).

[11] Y. Q. Ye, Y. Jin, and S. He "Omnidirectional, polarization-insensitive and broadband thin absorber in the terahertz regime," *JOSA B* **27**, pp. 498-504 (2010).

[12] C. Wu, B. Neuner III, G. Shvets, J. John, A. Milder, B. Zollars, and S. Savoy, "Large-area wide-angle spectrally selective plasmonic absorber," *Phys. Rev. B* **84**, p. 075102 (2011).

[13] B. Zhang, Y. Zhao, Q. Hao, B. Kiraly, I. C. Khoo, S. Chen, and T. J. Huang "Polarization-independent dual-band infrared perfect absorber based on a metal-dielectric-metal elliptical nanodisk array," *Opt. Express* **19**, pp. 15221-15228 (2011).

[14] K. Chen, T. D. Dao, S. Ishii, M. Aono, and T. Nagao, "Infrared aluminum metamaterial perfect absorbers for plasmon-enhanced infrared spectroscopy," *Adv. Funct. Mater.* **25**, pp. 6637-6643 (2015).

[15] Q. Feng, M. Pu, C. Hu, and X. Luo, "Engineering the dispersion of metamaterial surface for broadband infrared absorption," *Opt. Lett.* **37**, pp. 2133-2135 (2012).

[16] S. Shrestha, Y. Wang, A. C. Overvig, M. Lu, A. Stein, L. D. Negro, and N. Yu "Indium tin oxide broadband metasurface absorber," *ACS Photonics* **5**, pp. 3526-3533 (2018).

[17] N. Liu, M. MeschM, T. Weiss, M. Hentschel, and H. Giessen, "Infrared perfect absorber and its application as plasmonic sensor," *Nano. Lett.* **10**, pp. 2342-2348 (2010).

[18] A. Artar, A. A. Yanik, and H. Altug, "Fabry–pérot nanocavities in multilayered plasmonic crystals for enhanced biosensing," *Appl. Phys. Lett.* **95**, p. 051105 (2009).

[19] X. Lu, R. Wan, and T. Zhang, "Metal-dielectric-metal based narrow band absorber for sensing applications," *Opt. Express* **23**, pp. 29842-29847 (2015).

[20] M. Hentschel, T. Weiss, S. Bagheri, and H. Giessen, "Babinet to the half: coupling of solid and inverse plasmonic structures,"*Nano. Lett.* **13**, pp. 4428-4433 (2013).

[21] B. X. Wang, G. Z. Wang, and L. L. Wang, "Design of a novel dual-band terahertz metamaterial absorber," *Plasmonics* **11**, pp. 523-530 (2016).

[22] T. D. Dao, A. T. Doan, D. H. Ngo, K. Chen, S. Ishii, A. Tamanai, and T. Nagao "Selective thermal emitters with infrared plasmonic indium tin oxide working in the atmosphere," *Opt. Mater. Express* **9**, pp. 2534-2544 (2019).

[23] T. D. Dao, K. Chen, S. Ishii, A. Ohi, T. Nabatame, M. Kitajima, and T. Nagao, "Infrared perfect absorbers fabricated by colloidal mask etching of Al–Al2O3–Al trilayers," *ACS Photonics* **2**, pp. 964-970 (2015).

[24] J. A. D'Archangel, D. J. Shelton, R. Hudgins, M. K. Poutous, and G. D. Boreman, "Large area infrared frequency selective surface with dimensions reproducible by optical lithography," *J. Vac. Sci. Technol. B* **32**, p. 051807 (2014).

[25] H. T.Chen, "Interference theory of metamaterial perfect absorbers," *Opt. Express* **20**, pp. 7165-7172 (2012).

[26] Y. Li, D. Fullager, E. Angelbello, D. Childers, G. Boreman, and T. Hofmann, "Broadband near-infrared antireflection coatings fabricated by three-dimensional direct laser writing," *Opt. Lett.* **43**, pp. 239-242 (2018).

[27] Y. Li, S. Park, M. McLamb, M. Lata, S. Schöche, D. Childers, I. Aggarwal, M. Poutous, G. Boreman, and T. Hofmann, "UV to NIR optical properties of IP-Dip, IP-L, and IP-S after two-photon polymerization determined by spectroscopic ellipsometry," *Opt. Mater. Express* **9**, pp. 4318-4328 (2019).

[28] Y. Li, D. Fullager, S. Park, D. Childers, R. Fesperman, G. Boreman, and T. Hofmann, "High-contrast infrared polymer photonic crystals fabricated by direct laser writing," *Opt. Lett.* **43** pp. 4711-4714 (2018).

[29] D. B. Fullager, G. D. Boreman, and T. Hofmann, "Infrared dielectric response of nanoscribe IP-Dip and IP-L monomers after polymerization from 250 cm^{-1} to 6000 cm^{-1}," *Opt. Mater. Express* **7**, pp. 888-894 (2017).

[30] L. J. Sherry, S. H. Chang, G. C. Schatz, R. P. Van Duyne, B. J. Wiley, and Y. Xia, "Localized surface plasmon resonance spectroscopy of single silver nanocubes," *Nano. Letters* **5**, pp. 2034-2038 (2005).

[31] J. Becker, A. Trügler, A. Jakab, U. Hohenester, and C. Sönnichsen, "The optimal aspect ratio of gold nanorods for plasmonic bio-sensing," *Plasmonics* **5**, pp. 161-167 (2010).

[32] Y. Lee, S. J. Kim, H. Park, and B. Lee, "Metamaterials and metasurfaces for sensor applications," *Sensors* **17** p. 1726 (2017).

[33] B. X. Wang, G. Z. Wang, and T. Sang, "Simple design of novel triple-band terahertz metamaterial absorber for sensing application," *J. Phys. D Appl. Phys.* **49**, p. 165307 (2016).

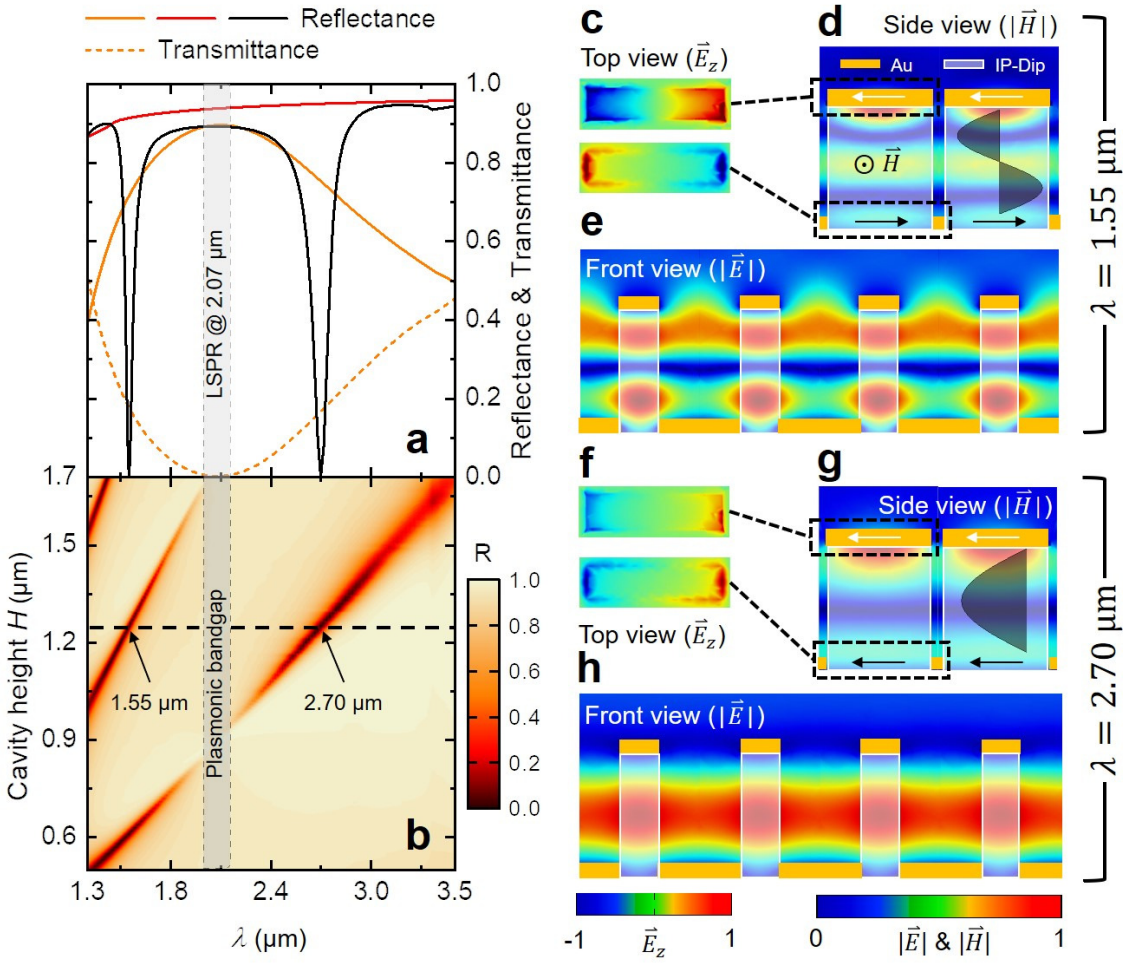

Figure 4.2: (a) Numerically calculated reflectance (solid) and transmittance (dotted) of the optimized reciprocal plasmonic metasurface (black) and its individual constituent parts: Au bar-antenna array (orange) and perforated film (red). (b) Numerically determined reflectance map of the reciprocal metasurface as a function of the height H of the fins valued from 0.5 µm to 1.7 µm. Panel (c) and (d) display the normalized electric field distributions $|\vec{E}|$ at the resonant wavelengths of 1.55 µm and 2.70 µm, respectively, as indicated by the black dashed line in panel (b). Panels (c) - (e) and (f) - (h) depict a second-order harmonic and fundamental harmonic standing wave for the wavelengths of 1.55 µm and 2.70 µm, respectively.

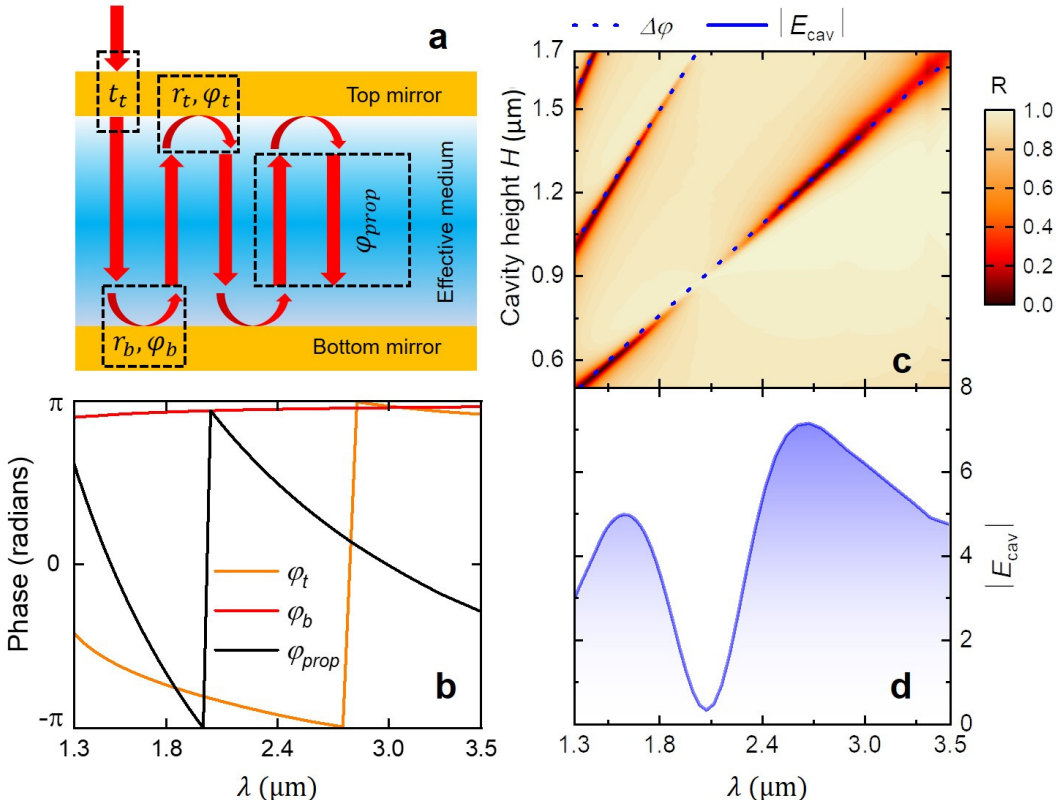

Figure 4.3: (a) Effective medium optical model of the optimized reciprocal metasurface consists of an effective medium sandwiched between two effective mirrors. Panel (b) shows phase changes at the mirrors (φ_t,φ_b) and due to the propagation (φ_{prop}). (c) Calculated resonant wavelengths (black dashed lines) with varying quantities of the cavity height H from 0.5 μm to 1.7 μm, wherein the numerically determined reflectance map shown in Fig. 4.2 (b) is shown for comparison. Panel (d) shows the calculated relative amplitude of the confined electric field $|E_{cav}|$ inside the effective medium.

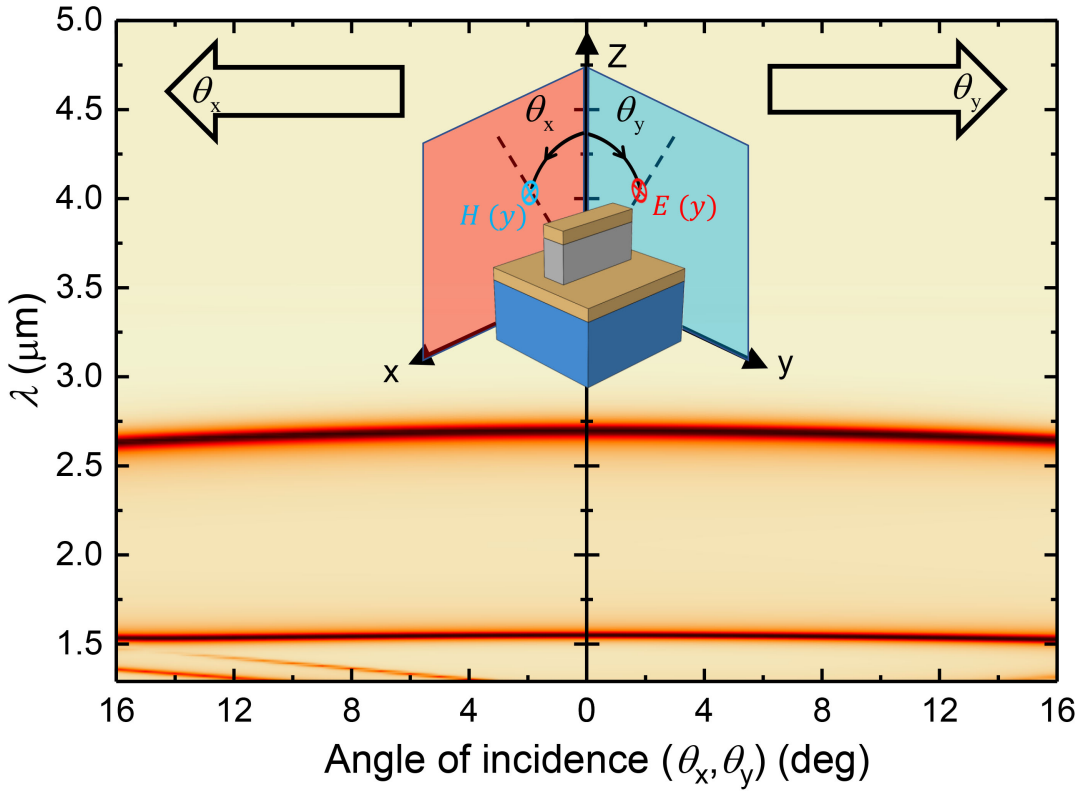

Figure 4.4: Angle of incident-dependent reflectance map calculated for a cavity height H=1.25 μm for an incidence defined by the angles θ_x and θ_y along the x- and y-axis, respectively. The polarization direction of the electric field is always parallel to the x-z plane. The dispersion of the cavity modes can be clearly observed.

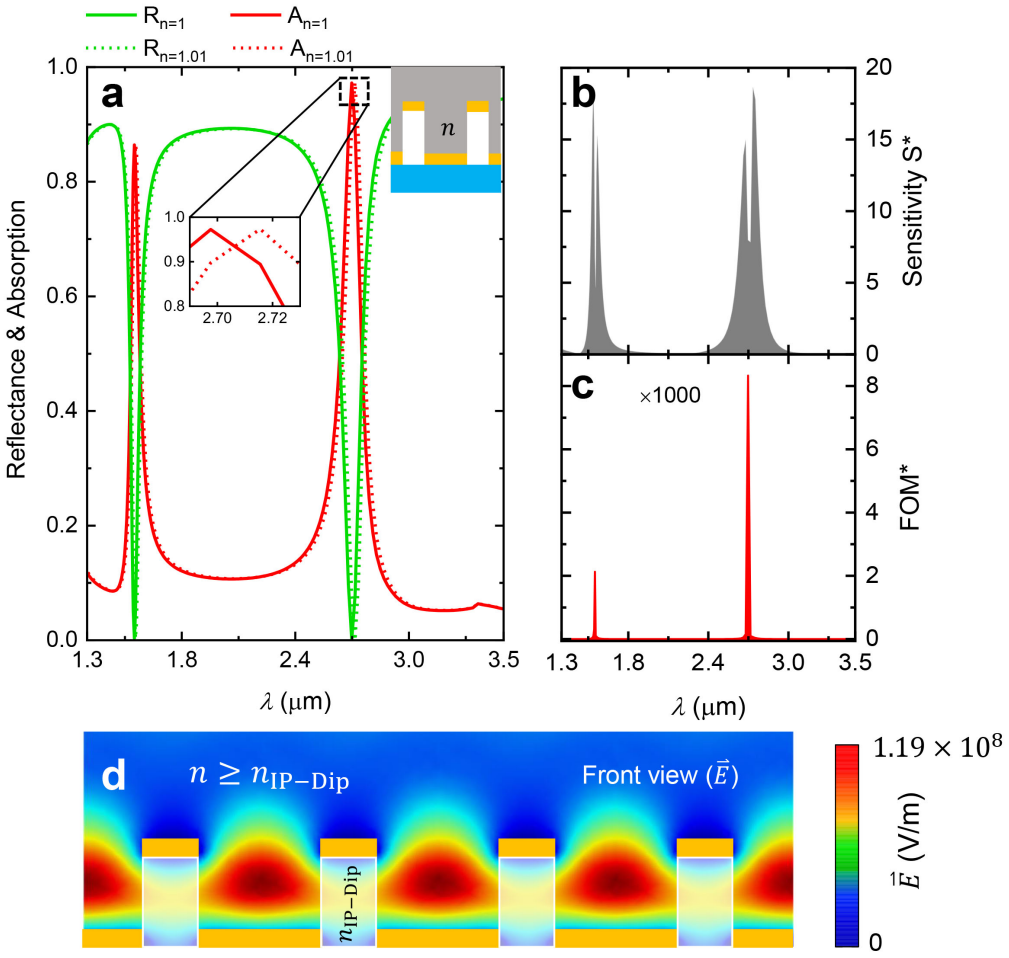

Figure 4.5: (a) Nearly perfect absorption with a Q-factor of 20 is obtained at the resonant wavelength of 2.70 µm (red solid line). As ambient index n, as shown in the inset, deviates from 1 to 1.01, the resonance peak at 2.70 µm has a 0.02 µm red shift (red dashed line), shown in the zoomed-in plot. The sensitivity S* and figure of merit FOM* are shown in (b) and (c) for characterizing the sensing capability of the reciprocal plasmonic metasurface. Panel (d) indicates the electric field $\vec{E}$ strongly localized between the polymer fins when $n \geq n_{\text{IP-Dip}}$.

CHAPTER 5: Tuning of reciprocal plasmonic metasurface resonances by ultra-thin conformal coatings

5.1 Overview

Metamaterials, in the form of perfect absorbers, have recently received attention for sensing and light-harvesting applications.[1] The fabrication of such metamaterials involves several process steps and can often lead to nonidealities, which limit the performance of the metamaterial. A novel reciprocal plasmonic metasurface geometry composed of two plasmonic metasurfaces separated by a dielectric spacer was developed and investigated here. This geometry avoids many common fabrication-induced nonidealities by design and is synthesized by a combination of two-photon polymerization and electron-beam-based metallization. Infrared reflection measurements revealed that the reciprocal plasmonic metasurface is very sensitive to ultra-thin, conformal dielectric coatings. This is shown here by using Al_2O_3 grown by atomic layer deposition. It was observed experimentally that incremental conformal coatings of amorphous Al_2O_3 result in a spectral red shift of the absorption band of the reciprocal plasmonic metasurface. The experimental observations were corroborated by finite element model calculations, which also demonstrated a strong sensitivity of the reciprocal plasmonic metasurface geometry to conformal dielectric coatings. These coatings therefore offer the possibility for post-fabrication tuning of the reciprocal plasmonic metasurface resonances, thus rendering this novel geometry as an ideal candidate for narrow-band absorbers, which allow for cost-effective fabrication and tuning.

[1]Reprinted by permission from MDPI M. McLamb, S. Park, V. P. Stinson, Y. Li, N. Shuchi, G. D. Boreman, and T. Hofmann, "Tuning of reciprocal plasmonic metasurface resonances by ultra-thin conformal coatings," *Optics* **3**, 70-78 (2022).

5.2 Introduction

Optical metamaterials are a group of engineered materials that are composed of an arrangement of artificial structures, which result in properties that are not exhibited in naturally occurring compounds [1, 2]. These unique optical properties can be used to produce extraordinary optical effects including giant optical activity [3, 4], narrow band filters [5, 6], perfect lensing [7, 8], and perfect absorption [9, 10], to name only a few of the most prominent, well-documented effects. In addition to enabling novel optical components and devices, the optical properties of metamaterials can be carefully tailored to the requirements of the application by changing the composition, geometry, and arrangement of the constituents [11].

Metamaterials with perfect absorption have attracted much attention as they allow the design of novel sensors for the detection of trace gasses [12, 13, 14, 15], are used for increasing the efficiency of solar cells [16, 17], and are also used as optical switches [18, 19], for instance. In order to achieve perfect absorption, metamaterial designs that rely on heterostructures have shown promising results. These materials are composed of multiple, stratified constituents [9, 10, 13, 20, 21, 14, 15, 22, 23, 24, 25, 26, 27, 28].

The fabrication of metamaterials requires complex nanofabrication techniques; for instance, colloidal lithography, nanosphere lithography, or focused ion beam writing are most frequently employed [25, 26, 27, 28, 29, 30, 31, 33, 32]. Due to the complexity of the fabrication processes, deviations from nominal geometries are often inevitable. One of the sources of such deviations that can result in a substantial degradation of the optical response of the heterostructure is the alignment of the metamaterial components. Thus, the identification of metamaterial geometries and fabrication approaches that eliminate these nonidealities are of critical importance.

In addition, toward the goal of realizing metamaterial designs that avoid crucial fabrication steps or simplify the fabrication process, metamaterials that allow the adjustment of the optical response by using simple, scalable sample size post-fabrication

processes could lead to a substantial reduction in the fabrication time and materials. The central idea is that small adjustments in the optical response of the metamaterial may be accomplished without a change in the overall geometry of the metasurface. These small adjustments can instead be made by using a comparatively simple post-fabrication approach in which the metasurface is conformally coated with a dielectric [34].

We developed a reciprocal plasmonic metasurface geometry that simplifies the fabrication process of heterostructured metamaterials and thereby prevents nonidealities by avoiding the misalignment of the metasurface constituents by design [24]. Reciprocal plasmonic metasurfaces are composed of two plasmonic metasurfaces with reciprocal surface geometries that are separated by a dielectric spacer. We explored the optical response of reciprocal metasurfaces theoretically using finite element calculations and found that the geometry enables a post-fabrication adjustment of its spectral response by applying a thin conformal dielectric coating [24].

In this paper, we demonstrate for the first time that reciprocal plasmonic metasurfaces can be fabricated using two-photon polymerization techniques in combination with a simple metallization using electron-beam evaporation. The fabrication process, using only two main process steps, eliminates the requirement of crucial alignment steps between the top and bottom metasurface.

We further explored the effect of subsequent ultra-thin conformal dielectric coatings on the spectral response of the reciprocal plasmonic metasurface. Our observations indicated that such dielectric coatings can induce a spectral red-shift of the main resonance of the reciprocal plasmonic metasurface, corroborating our previous theoretical findings.

5.3 Materials and Methods

A schematic of the unit cell of the investigated reciprocal plasmonic metasurface can be seen in Figure 5.1.

The reciprocal plasmonic metasurface was composed of a rectangular Au bar array separated by a dielectric spacer from a rectangular hole array. A negative-tone photoresist polymer (IP-Dip), which is compatible with two-photon polymerization, was used as a dielectric spacer. Fused silica glass was employed as a substrate. The infrared optical response of the reciprocal plasmonic metasurface was calculated using finite element modeling (FEM) simulations through COMSOL. The calculations were performed for the wavelength range from 4 µm to 7 µm using periodic boundary conditions along a unit cell. Accurate dielectric function data for fused silica glass and IP-Dip were obtained using spectroscopic ellipsometry in the range from 2 µm to 33 µm and were used for the FEM calculations [33, 35, 36].

The effect of a conformal dielectric coating of amorphous Al_2O_3 on the spectral response of the reciprocal plasmonic metasurface was investigated for four different coating thicknesses: 10 nm, 20 nm, 30 nm, and 40 nm. A simple harmonic oscillator approach consisting of six Gaussian oscillators was used to describe the optical properties of the amorphous Al_2O_3 grown using atomic layer deposition. The real and imaginary parts of the model dielectric function $\varepsilon_1(\lambda)$ and $\varepsilon_2(\lambda)$, respectively, used for the COMSOL calculations can be seen in Figure 5.2. A summary of the parameterized Gaussian oscillators can be found in Table 5.1.

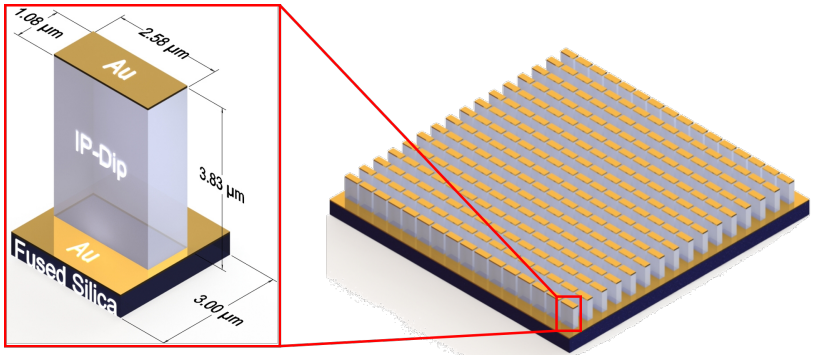

Figure 5.1: Depiction of the square unit cell used in COMSOL modeling. The metasurface is composed of three layers: an IP-Dip polymer fin, a 50 nm Au dipole layer atop the fin, and a 50 nm layer surrounding the base of the fin. Fused silica is used as a substrate.

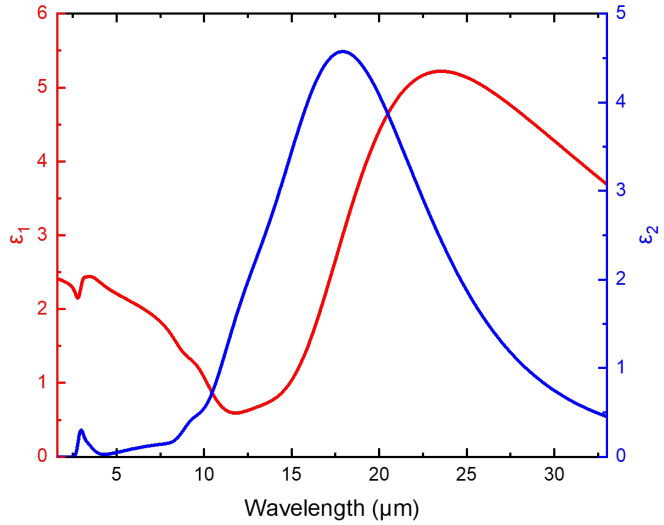

Figure 5.2: Real $\varepsilon_1(\lambda)$ and imaginary $\varepsilon_2(\lambda)$ part of the model dielectric function of amorphous Al_2O_3 in the spectral range of 2 µm to 33 µm used for the COMSOL calculations reported here. The model dielectric function is composed of six Gaussian oscillators with the parameters summarized in Table 5.1.

Table 5.1: Amplitude, center energy, and broadening parameters of the six Gaussian oscillators used to characterize amorphous Al_2O_3 in the wavelength range from 2 µm to 33 µm.

Amplitude	**Energy (cm^{-1})**	**Broadening (cm^{-1})**
4.081	541.8	256.7
1.624	766.9	294.7
0.1803	1075	155.2
0.1727	891.7	1631
0.1529	3067	703.4
0.2141	3407	390.5

The reciprocal plasmonic metasurfaces investigated here were fabricated using a two-step process: two-photon polymerization followed by metallization, depicted in Figure 5.3.

Prior to the two-photon polymerization step, the substrate was cleaned by rinsing with isopropanol-2, drying with N_2, followed by a 5 min plasma cleaning using 12

SCCM flow of O_2 at 13.56 MHz with a power of 150 W. The polymerization process was performed using a commercial two-photon lithography system (Photonic Professional GT, Nanoscribe GmbH), which employs a 780 nm femtosecond laser with an inverted microscope.

A 63× microscope objective was directly immersed into the monomer for the polymerization of a rectangular fin array, as shown in Figure 5.3. The laser beam position in the sample plane was controlled through a galvanometer. The position of the laser beam normal to the sample plane was controlled via a piezo actuator. To ensure structure quality and promote adhesion of the polymer to the substrate, the exposure parameters were optimized by adjusting the laser power and write speed prior to the sample fabrication. After polymerization was completed, the excess monomer was removed by immersing the sample into propylene glycol monomethyl ether acetate followed by isopropanol-2 for five minutes each. Once the excess monomer had been removed, the sample was allowed to air dry at room temperature for approximately 5 min.

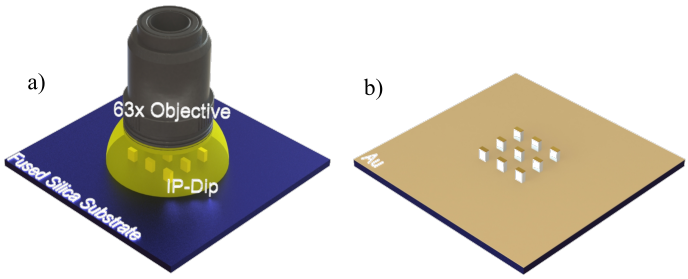

Figure 5.3: A schematic of the two-step fabrication method used to synthesize reciprocal plasmonic metasurfaces is shown. (**a**) Initially, rectangular fin arrays are additively manufactured using two-photon polymerization on a fused silica substrate. (**b**) Post-polymerization, the reciprocal metasurface sample is metalized using electron beam evaporation, simultaneously forming the top and bottom layers of the sample.

Subsequent to the direct laser writing of the fin structures, the sample was metalized using an electron beam deposition system (Kurt J. Lesker PVD 75). A 5 nm layer of Cr, sourced from Cr pieces (99.95%), and a 50 nm Au layer, evaporated from Au

pellets (99.99%), were deposited at a rate of 1 Å/s and 3 Å/s, respectively. The metallization resulted in the formation of a reciprocal plasmonic metasurface (see Figure 5.1). A rectangular bar array was placed on the top of the dielectric fins and a rectangular hole array on the substrate surrounding the bottom of the dielectric fins. All depositions were conducted at room temperature at a pressure of 2.53×10^{-5} Pa. The substrate holder was rotated during the deposition at approximately 15 rotations per minute to ensure a homogeneous film thickness across the sample.

The metasurface was characterized using polarized infrared reflection measurements to determine its infrared optical response. Linearly polarized reflectance spectra were captured using a Hyperion 3000 microscope (Bruker) in combination with a Vertex 70 FTIR spectrometer (Bruker). The reflectance measurements were carried out in the spectral range 4 µm to 7 µm with a resolution of 0.05 µm. A 15× IR Schwarzschild objective and 20 µm × 20 µm aperture, resulting in an average angle of incidence of 8.7°, was used in combination with a mercury cadmium telluride detector for all infrared reflection measurements. A wire-grid polarizer mounted in a rotation stage was used to polarize the incident radiation.

In order to experimentally explore the effect of ultra-thin conformal dielectric coatings on the spectral location of the reciprocal plasmonic metasurface resonance, Al_2O_3 coatings were deposited using atomic layer deposition (Cross flow Savannah G2) in 10 nm thickness increments up to 40 nm. The depositions were carried out at 80 °C using trimethylaluminum (TMA) as a precursor and H_2O as an oxidizer. The chamber pressure was kept at 10.7 Pa. Alternating 0.015 s-long pulses of TMA and H_2O were used to grow the Al_2O_3 film with a growth rate of 0.8 Å/cycle. The growth rate was determined using ex situ spectroscopic ellipsometry in the visible spectrum. Four subsequent depositions of 10 nm films were grown with one-hundred twenty-five cycles each. Infrared reflectance measurements were conducted between each iteration to characterize the spectral response of the metasurface. COMSOL-based FEM model

calculations were carried out for the corresponding conformal coating thicknesses for the comparison with the experimental infrared reflectance data.

5.4 Results and Discussion

Figure 5.4 shows the experimental reflectance spectrum of the as-fabricated reciprocal plasmonic metasurface without any dielectric coating. The incident radiation was polarized along the long axis of the rectangular dipoles forming the top metasurface, as shown in Figure 5.1. The reflectance spectra were dominated by a reflection minimum with a center wavelength of 4.8 µm. This reflectance minimum was due to a resonant absorption caused by the reciprocal plasmonic metasurface at that wavelength. A second, much smaller reflection minimum, could be observed at 5.8 µm. This feature was due to an absorption band of IP-Dip, which was used as a dielectric spacer in the reciprocal plasmonic metasurface and can be easily recognized in the imaginary part of the dielectric function of the polymerized IP-Dip reported earlier [35].

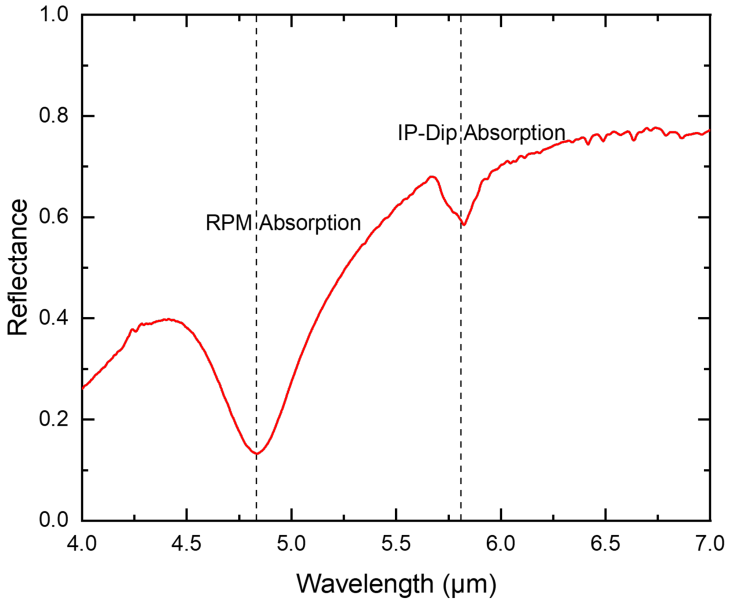

Figure 5.4: Experimental reflectance spectrum of the fabricated reciprocal plasmonic metasurface without any dielectric coating. The experimental data were obtained at 8.7° incidence with a polarization parallel to the long axis of the rectangular fins. The resonance of the reciprocal plasmonic metasurface can be observed at 4.8 µm. The absorption feature, located at 5.8 µm, is due to an absorption band in the dielectric spacer (see Figure 5.1) [35].

The origin of the absorption in reciprocal plasmonic metasurfaces was investigated theoretically using FEM and analytical effective-medium-based calculations in [24]. These calculations indicated that a constructive interference within the dielectric spacer can be formed due to the coupling between the top and bottom metasurfaces. The FEM calculations further indicated that the field enhancement between the dielectric spacer fins resulted in the extreme sensitivity of the optical response to minute and local ambient index changes [24].

It can be noted that the overall amplitude of the experimental reflection spectrum presented in Figure 5.4 was lower than what was reported in [24] obtained from FEM calculations assuming an ideal reciprocal metasurface geometry. We tentatively attributed this deviation in the reflection amplitude to imperfections in the reciprocal metasurface geometry.

The metasurface was coated by subsequent conformal layers of Al_2O_3 at 10 nm per iteration to monitor the effect of these thin dielectric coatings on the reciprocal plasmonic metasurface resonance. The thickness of each subsequent dielectric coating was monitored using a witness sample, which was characterized by ex situ spectroscopic ellipsometry. The reflectance measurements were performed between each deposition starting at a coating thickness of 10 nm. The radiation was incident to the sample plane at 8.7° and polarized along the long axis of the top dipole layer.

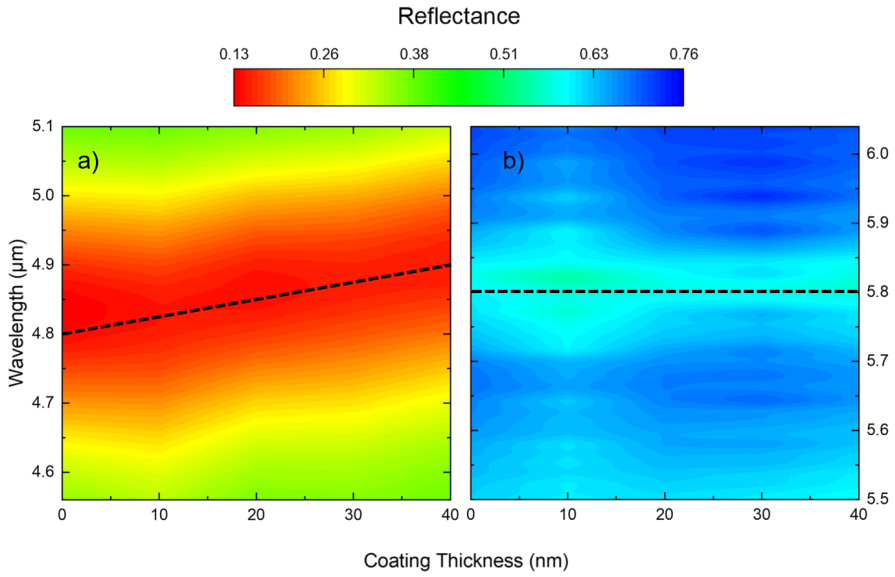

Figure 5.5: False-color map of the reflectance of the reciprocal plasmonic metasurface as a function of the coating thickness and wavelength centered on the plasmonic metasurface resonance (**a**) and the IP-Dip absorption band (**b**), respectively. Whereas a shift of the center absorption wavelength as a function of dielectric coating thickness can be easily observed in (**a**), the IP-Dip absorption band shown in (**b**) is not affected, as expected.

Figure 5.5 shows the experimental reflectance as a function of wavelength and coating thickness in the spectral vicinity of the reciprocal plasmonic metasurface resonance (a) and the IP-Dip absorption band (b) for comparison. Figure 5.5a clearly shows that the reflectance minimum associated with the reciprocal plasmonic metasurface resonance followed a linear spectral shift from $\lambda = 4.8$ µm for the uncoated sample to $\lambda = 4.9$ µm for a coating thickness of 40 nm. In comparison, the IP-Dip absorp-

tion band depicted in Figure 5.5b did not shift as a function of the Al_2O_3 coating thickness. This was as expected, because this is an intrinsic property of polymerized IP-Dip.

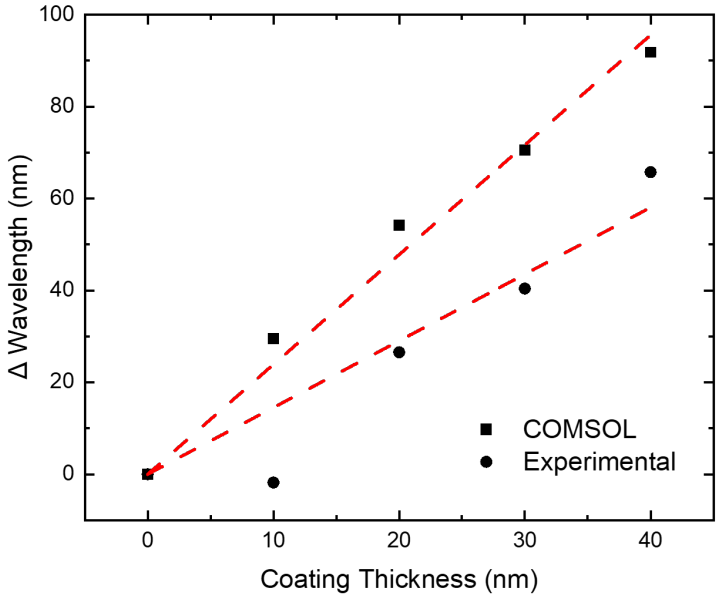

Figure 5.6: Experimental results delineating the effects of incremental conformal coatings of amorphous Al_2O_3 deposited on reciprocal plasmonic metasurfaces. The main absorption peak represented in Figure 5.4 at 4.8 µm red-shifts after 10 nm increments.

Figure 5.6 illustrates the experimentally observed wavelength shift of the reciprocal plasmonic metasurface resonance in comparison to the FEM-based model calculations (COMSOL). A linear trend can be recognized in the experimental data, as well as in the numerical simulations. We determined the slope of the wavelength shift for the experimental data to be 1.5, which is only sightly smaller than the slope of 2.4 for the data obtained using the numerical calculations. It can be further noticed that while the numerical calculations increased monotonically, the first experimental data point obtained for a thickness of 10 nm was virtually identical to the one obtained for the uncoated reference measurement. We tentatively attributed this behavior to the non-conformal coating of the reciprocal plasmonic metasurface. This could be caused by the high aspect ratio of the dielectric spacer fins, approximately 3:2 and 7:2 for

the long and short axes, respectively. Initial growth delay was observed for atomic layer deposition on planar surfaces; however, the impact of the surface topology on the growth rate is not well known.

5.5 Conclusions

Reciprocal plasmonic metasurfaces were experimentally demonstrated and characterized for the first time. The samples were synthesized using a two-step fabrication process. In the first step, two-photon lithography was used to deposit dielectric spacer fins. During the second step, electron beam evaporation of Au was employed to metalize the top of the dielectric spacers and the substrate surface, thereby forming two plasmonic metasurfaces with reciprocal geometries. This two-step fabrication technique is advantageous, as it ensures the alignment of the reciprocal surfaces by design.

Experimental infrared reflection measurements revealed the expected reciprocal plasmonic metasurface resonance, which was observed for the investigated geometries at 4.8 µm. The location of this resonance was confirmed using finite element calculations. After incremental conformal coatings of the reciprocal plasmonic metasurface with Al_2O_3 using atomic layer deposition, a shifting of the resonance wavelength was observed. It was found that the wavelength shift depended linearly on the Al_2O_3 coating thickness. The reciprocal plasmonic metasurface geometry therefore offers the tunability of the absorption wavelength through a thin conformal coating of a dielectric.

To conclude, the reciprocal plasmonic metasurface provides a novel geometry for scalable and tunable metamaterials. The simple configuration and sensitivity to thin conformal dielectric films demonstrated the reciprocal plasmonic metasurface as an adaptable platform for the rapid prototyping. In addition, the conformal dielectric coatings were shown to enable the adjustment of the metasurface resonances.

REFERENCES

[1] W. Cai and V. M. Shalaev, "*Optical Metamaterials*," Springer Science (2010).

[2] A. K. Sarychev and V. M. Shalaev, "*Electrodynamics of Metamaterials*," World Scientific (2007).

[3] E. Plum, V. A. Fedotov, and N. I. Zheludevb, "Optical activity in extrinsically chiral metamaterial," *Appl. Phys. Lett.* **93**, p. 191911 (2008).

[4] M. Decker, R. Zhao, C. M. Soukoulis, S. Linden, and M. Wegener, "Twisted split-ring-resonator photonic metamaterial with huge optical activity," *Opt. Lett.* **35**, pp. 1593-1595 (2010).

[5] V. P. Stinson, S. Park, M. McLamb, G. Boreman, and T. Hofmann, "Photonic Crystals with a Defect Fabricated by Two-Photon Polymerization for the Infrared Spectral Range," *Optics* **2**, pp. 284-291 (2021).

[6] A. H. Aly, H. A. Elsayed, and C. Malek, "Defect modes properties in one-dimensional photonic crystals employing a superconducting nanocomposite material," *Opt. Appl.* **48**, pp. 53-64 (2018).

[7] J. B. Pendry and S. A. Ramakrishna, "Refining the perfect lens," *Physica B* **338**, pp. 329-332 (2013).

[8] M. Tsang and D. Psaltis, "Magnifying perfect lens and superlens design by coordinate transformation," *Phys. Rev. B 77*, p. 035122 (2008).

[9] D. Wu, Y. Liu, R. Li, L. Chen, R. Ma, C. Liu, and H. Ye, "Infrared perfect ultra-narrow band absorber as plasmonic sensor," *Nanoscale Res. Lett.* **11**, p. 483 (2016).

[10] A. Ghobadi, H. Hajian, A. R. Rashed, B. Butun, and E. Ozbay, "Tuning the metal filling fraction in metal-insulator-metal ultra-broadband perfect absorbers to maximize the absorption bandwidth," *Photonics Res.* **6**, pp. 168-176 (2018).

[11] Y. Liu and X. Zhan, "Metamaterials: a new frontier of science and technology," *Chem. Soc. Rev.* **40**, pp. 2494-2507 (2011).

[12] N. Liu, M. Mesch, T. Weiss, M. Hentschel, and H. Giessen, "Infrared Perfect Absorber and Its Application As Plasmonic Sensor," *Nano Lett.* **10**, pp. 2342–2348 (2010).

[13] R. Ameling, L. Langguth, M. Hentschel, M. Mesch, P. V. Braun, and H. Giessen, "Cavity-enhanced localized plasmon resonance sensing," *Appl. Phys. Lett.* **97**, p. 253116 (2019).

[14] T. Pohl, F. Sterl, N. Strofeldt, and H. Giessen, "Optical Carbon Dioxide Detection in the Visible Down to the Single Digit ppm Range Using Plasmonic Perfect Absorbers," *ACS Sens.* **5**, pp. 2628-2635 (2020).

[15] L. Shi, J. Shang, Z. Liu, Y. Li, G. Fu, X. Liu, P. Pan, H. Luo, and G. Liu, "Ultra-narrow multi-band polarization-insensitive plasmonic perfect absorber for sensing," *Nanotechnology* **31**, p. 465501 (2020).

[16] B. Mulla and C. Sabah, "Perfect metamaterial absorber design for solar cell applications," *Wave Random Complex* **25**, pp. 382-383 (2015).

[17] S. A. Mann and E. C. Garnett, "Resonant Nanophotonic Spectrum Splitting for Ultrathin Multijunction Solar Cells," *ACS Photonics* **2**, pp. 816-821 (2015).

[18] N. Zheludev and Y. Kivshar, "From metamaterials to metadevices," *Nature Mater.* **11**, pp. 917-924 (2012).

[19] Z. Qian, S. Kang, V. Rajaram, C. Cassella, N. E. McGruer, and M. Rinaldi, "Zero-power infrared digitizers based on plasmonically enhanced micromechanical photoswitches," *Nat. Nanotechnol.* **12**, pp. 969-973 (2017).

[20] Z. Song, K. Wang, J. Li, and Q.-H. Liu, "Broadband tunable terahertz absorber based on vanadium dioxide metamaterials," *Opt. Express* **27**, pp. 7148-7154 (2018).

[21] M. Masyukov, A. N. Grebenchukov, E. A. Litvinov, A. Baldycheva, A. V. Vozianova, and M. K. Khodzitsky, "Photo-tunable terahertz absorber based on intercalated few-layer graphene," *J. Opt.* **22**, p. 095105 (2020).

[22] T. D. Dao, A. T. Doan, D. H. Ngo, K. Chen, S. Ishii, A. Tamanai, and T. Nagao, "Selective thermal emitters with infrared plasmonic indium tin oxide working in the atmosphere," *Opt. Mater. Express* **9**, pp. 2534-2544 (2019).

[23] Y. Yao, J. Zhou, Z. Liu, X. Liu, G. Fu, and G. Liu, "Refractor materials and plasmonics based perfect absorbers," *Nanotechnology* **32**, p. 132002 (2021).

[24] Y. Li, M. McLamb, S. Park, D. Childers, G. Boreman, and T. Hofmann, "Theoretical Study of Enhanced Plasmonic-Photonic Hybrid Cavity Modes in Reciprocal Plasmonic Metasurfaces," *Plasmonics 16*, pp. 2241-2247 (2021).

[25] P. Karl, S. Mennle, M. Ubl, P. Flad, J.-W. Yang, T.-Y. Peng, Y.-J. Lu, and H. Giessen, "Niobium nitride plasmonic perfect absorbers for tunable infrared superconducting nanowire photodetection," *Opt. Express* **29**, pp. 17087-17096 (2021).

[26] N. To, S. Juodkazis, and Y. Nishijima, "Detailed Experiment-Theory Comparison of Mid-Infrared Metasurface Perfect Absorbers," *Micromachines-Basel* **11**, p. 409 (2020).

[27] G. O. Bonin, S. J. Barrow, T. U. Connell, A. Roberts, A. S. R. Chesman, D. E. Gómez, "Self-Assembly of Plasmonic Near-Perfect Absorbers of Light: The Effect of Particle Size," *J. Phys. Chem. Lett.* **11**, pp. 8378-8385 (2020).

[28] M. Hentchel, T. Weiss, S. Bagheri, and H. Giessen, "Babinet to the Half: Coupling of Solid and Inverse Plasmonic Structures," *Nano Lett.* **13**, pp. 4428-4433 (2013).

[29] V.-C. Su, C. H. Chu, G. Sun, and D. P. Tsai, "Advances in optical metasurfaces: fabrication and applications," *Opt. Express* **26**, pp. 13148-13182 (2018).

[30] P. Genevet, F. Capasso, F. Aieta, M. Khorasaninejad, R. Devlin, "Recent advances in planar optics: from plasmonic to dielectric metasurfaces," *Opt.* **4**, pp. 139–152 (2017).

[31] W. Wang, M. Ramezani, A. I. Väkeväinen, P. Törmä, J. G. Rivas, T. and W. Odom, "The rich photonic world of plasmonic nanoparticle arrays," *Mater. Today* **21**, pp. 303-314 (2018).

[32] T. D. Dao, K. Chen, S. Ishii, A. Ohi, T. Nabatame, M. Kitajima, and T. Nagao, "Infrared Perfect Absorbers Fabricated by Colloidal Mask Etching of Al-Al_2O_3-Al Trilayers," *ACS Photonics* **2**, pp. 964-970 (2015).

[33] M. McLamb, Y. Li, P. Stinson, and T. Hofmann, "Metasurfaces for the infrared spectral range fabricated using two-photon polymerization," *Thin Solid Films* **721**, p. 138548 (2021).

[34] D. Franklin, M. George, J. Fraser, and D. Chanda, "Atomic layer deposition tuning of subwavelength aluminum grating for angle-insensitive plasmonic color," *ACS Appl. Nano Mater.* **1**, pp. 5210-5216 (2018).

[35] D. B. Fullager, G. D. Boreman, and T. Hofmann, "Infrared dielectric response of nanoscribe IP-dip and IP-L monomers after polymerization from 250 cm^{-1} to 6000 cm^{-1}," *Opt. Mater. Express* **7**, pp. 888-894 (2021).

[36] Y. Li, S. Park, M. McLamb, M. Lata, S. Schöche, D. Childers, I. D. Aggarwal, M. K. Poutous, G. Boreman, and T. Hofmann, "UV to NIR optical properties of IP-Dip, IP-L, and IP-S after two-photon polymerization determined by spectroscopic ellipsometery," *Opt. Mater. Express* **9**, pp. 4318-4328 (2019).

CHAPTER 6: Conclusion

We have shown that a novel rapid prototyping technique for the additive manufacturing of plasmonic metamaterials using two-photon polymerization is possible. This was demonstrated by fabricating several plasmonic metamaterial samples including polarization sensitive filters, polarization sensitive images encoded onto a surface, and a perfectly absorbing metamaterial with sensitivity to changes in ambient index. All fabricated samples were first simulated using finite element modeling with good agreement found between experimental and simulated data.

Initially, a dipole array with a polarization sensitive reflective response was fabricated as a proof of concept of the rapid prototyping technique and detailed in chapter 1. To fabricate the array, two-photon polymerization was used to create an inverse array using a compatible photoresin. The inverse array is then coated with Au using electron beam physical vapor deposition. Finally, the inverse polymer layer is lifted off using a combination of rinsing with solvents and plasma cleaning leaving only the desired structures left behind. This fabrication technique allows for nearly arbitrary two-dimensional plasmonic geometries.

This dipole array was later modified with a set of two encoded images where the image displayed depended on the linear input polarization. This is done by rearranging the metallic elements to produce an image with sufficient contrast between the reflectance obtained from the change in polarization states.

The natural progression from two-dimensional materials would be more complex structures in the form of three-dimensional metamaterials. The reciprocal plasmonic metasurface is a metal-insulator-metal configured material displaying theoretical perfect absorption with the same basic design as the dipole array but with the inclusion

of a dielectric scaffold. This scaffold acts as a separator of the top and bottom metallic layers. The electromagnetic field enhancement between the top and bottom layers due to plasmonic resonance interact with each other within this separation layer leading to enhanced absorption.

The enhancement due to plasmonic effects not only leads to strong absorption effects but also allows for an extreme sensitivity to changes in the ambient refractive index. Sensitivity was initially simulated using finite-element modeling software and shifting the background index of air from 1 to 1.01 resulting in a shift of the absorption wavelength by .02 µm. To show this experimentally, conformal coatings of Al_2O_3were deposited on the reciprocal plasmonic metasurface using ALD in increments of 10 nm thickness. Effects of these coatings were also simulated using accurate dielectric function data obtained from spectroscopic ellipsometry and compared to experimental results. Simulated and experimental results showed good agreement with a linear trend, as expected when comparing to the simulated change in ambient refractive index.

In addition to plasmonic metamaterials it is suggested that the inclusion of phase change materials be investigated. The incorporation of conformal layers of vanadium dioxide would be compatible with polymer scaffolds and current fabrication capabilities. This would allow for dynamic modulation of the optical properties of the demonstrated designs.